

A Spherical Multipole Expansion of Acoustic Analogy for Propeller Noise

Felice Fruncillo^{1,2,†}, Paolo Luchini¹ and Flavio Giannetti¹

¹University of Salerno, Via Giovanni Paolo II, 132, Fisciano, 84084

²CIRA, Italian Aerospace Research Center, Via Maiorise, Capua, 81043

This work develops a spherical-multipole expansion of Goldstein's acoustic analogy, for the prediction of tonal noise from rotating propellers. The acoustic field is expressed through spherical multipoles, which separate source integrals from the observer dependence. This decoupling leads to computational efficiency: once the multipole coefficients are computed from blade geometry and aerodynamics, the sound field at any observer location is obtained by a simple evaluation of spherical harmonics and radial propagation factors, avoiding repeated integrations for each observer point. Moreover, this enables a straightforward radiated power calculation, without resorting to far-field pressure integrals. For hovering subsonic propellers, the results show a rapid convergence of the expansion. For each harmonic, the dominant radiation is accurately captured by the first two non-zero multipoles, corresponding to the leading symmetric and antisymmetric contributions with respect to the plane of rotation. To interpret the physical content of these leading terms, two simplified descriptions of the source integral are developed. The first is a lifting-surface formulation, suited to blades at small incidence, in which the thin-airfoil approximation allows to separate lift-like loading, drag-like loading, and thickness contributions. The second is a lifting-line formulation, suited to high-aspect-ratio blades, in which the surface integral is reduced to spanwise integrals of compact sectional moments. The validity of the two formulations is assessed through comparisons of directivity, power distribution over harmonics and time-domain waveforms. The results show good accuracy in their respective regimes of validity, together with substantial computational savings.

1. Introduction

The prediction of tonal noise from rotating blades is a long-standing problem in aeroacoustics. Early successful work by Gutin (1936) represented the propeller as a distribution of source forces acting on the rotor disk, yielding analytical expressions for the noise harmonics. In the following year, Deming (1937) identified the contribution of thickness noise, thereby correcting Gutin's results for blades operating at low incidence. A few years later, Garrick & Watkins (1954) extended these findings to account for a uniform mean flow.

As in many acoustic problems, progress was strongly influenced by the development of acoustic analogies. The classic theories initiated by Lighthill (1952) and Curle (1955) recast the fluid-dynamic equations into an inhomogeneous wave equation and represent the effect of solid boundaries through equivalent sources. From the outset, these approaches provided a prolific framework for propeller noise (Ffowcs Williams & Hawkins 1969; Morfey 1972; Hawkins & Lawson 1974). The Ffowcs Williams-Hawkins (FFW-H) equation (Ffowcs Williams & Hawkins 1969) generalized this framework to arbitrarily moving and permeable surfaces. Together with the time-domain integral formulations developed by Farassat (Farassat 1977, 1981), FFW-H became a standard reference for rotor-noise modelling. Time-domain methods are powerful for high-fidelity prediction, but they can be computationally demanding when

† Email address for correspondence: ffruncillo@unisa.it

the full-sphere directivity is required and, by integrating over the entire source, may obscure the relationship between a specific design feature and its acoustic consequence (Hanson & Fink 1979). For these reasons, in parallel with these developments, in the 1970s Hanson pursued frequency-domain approaches aimed at efficient evaluation and physical interpretability. His helicoidal-surface theory (Hanson 1980), based on Goldstein's analogy (Goldstein 1976), offered analytical expressions for propeller far-field tones. Relative to earlier models, this theory represented a significant generalization: it simultaneously accounts for finite chordwise extent, forward flight, and a more realistic geometric description by replacing the disk idealization with a helicoidal surface. The final expressions follow from a far-field expansion of the Green's function, in a spirit similar to that employed by Gutin (1936). Hanson later extended these results to the near field (Hanson 1985), building on a cylindrical-coordinate expansion of the Green's function (Hanson 1983). He noted that, relative to the far-field case, the near-field formulation introduces an additional integration that can be interpreted as a Fourier transform in the wavenumber. More complete reviews of these early developments can be found in Morfey (1973) and Farassat & Succi (1980).

Many early studies were therefore rooted in planform-based blade representations on which source distributions were prescribed. Further simplifications were often obtained through a ring approximation of the propeller disk (Gutin 1936; Garrick & Watkins 1954), in which the distributed sources are assumed to be concentrated at a particular radius. Subsequently, lifting-line descriptions for high-aspect-ratio propellers showed that the tonal sound field can be predicted directly from the spanwise lift distribution, with good agreement against more detailed computations and experimental data (Brouwer 1989, 1992). With these tools at disposal, other investigations addressed a range of complementary aspects, including the validity of linearized models in reproducing measured waveforms and directivities up to supersonic tip Mach numbers (Hanson 1976), the effect of particular blade geometries (Hanson & Fink 1979; Dobrzynski 1993), and the role of scattering by the hub and nearby airframe structures (Glegg 1991). For an in-depth review of these works, the reader is referred to Metzger (1995), which also highlights that, from the 1990s onward, research efforts increasingly shifted toward computational aeroacoustics codes rather than analytical studies of acoustic analogies. In parallel, developments have also focused on efficient numerical evaluation of radiation integrals. As already noted in Gutin (1936) and frequently exploited thereafter, far-field approximations offer the simplest reduction in computational complexity. This is due to the simplified structure of the radiated field in the far zone, which allows the observer dependence to be treated in a much simpler form. In the more general case, cylindrical-coordinate expansions have often been adopted (Schulten 1984; Glegg 1991; Hanson & Parzych 1993; Douglas Mast & Yu 2005; Carley 2006) to alleviate the cost of the underlying integrals, which are also frequently evaluated directly in their unexpanded form (Hanson 1976; Chapman 1993; Carley 1999). Inevitably, both near and far-field formulations in the literature lead to expressions in which the observer location appears inside the source integrals. Far-field assumption reduces the number of observer coordinates embedded in the integration, but it does not remove the dependence entirely. This becomes an important limitation when predictions are required at a large number of microphone locations, as is very common in practical applications. Contributions in this direction were provided by Parry & Crighton (1989) for subsonic conditions and by Crighton & Parry (1991) for supersonic one; however, these results are restricted to the limit of an infinite number of blades, in which Hanson's integrals can be approximated asymptotically. Despite the substantial body of work outlined above, there is therefore a need for a formulation in which the source integrals do not have to be recomputed for each observer position.

This paper develops a formulation to address this need. Starting from Goldstein's acoustic analogy, we retain its two surface source terms, namely the aerodynamic force per unit area and the surface normal velocity. The core of the approach is a spherical expansion of the free-

space Green's function (Jackson 1962), which leads to a spherical-multipole representation of the acoustic pressure valid in both the near and far field. A central feature of the resulting expression is the complete separation between source and observer dependence: the multipole coefficients depend only on blade geometry and aerodynamics, whereas the observer coordinates appear only through spherical harmonics and radial propagation factors. This separation makes the method computationally attractive, since the source-dependent coefficients are computed once and can then be reused to evaluate the acoustic field rapidly at arbitrary observer locations. In recent work, Fruncillo *et al.* (2025) applied the same idea to a Kirchhoff-Helmholtz formulation (Williams 1999) and showed that it can reduce the computational cost of far-field multi-microphone predictions by up to two orders of magnitude relative to Hanson's formulation (Hanson 1980). The present work differs from that study, since it is based directly on an acoustic-analogy formulation rather than on a potential-flow boundary integral. As a result, the source description retains explicitly the aerodynamic force term appearing in Goldstein's analogy. This makes it possible to examine the separate roles played by loading, thickness, and drag-related contributions in the multipole expansion of propeller noise, whereas the latter effects cannot be considered within the framework adopted previously. A further advantage emphasized here is that the spherical representation yields a direct expression for the radiated power, without the need for additional pressure integrations, which is especially attractive for design and optimization purposes.

The spherical-multipole formulation is firstly examined in its exact form, i.e. by evaluating the resulting coefficients on the true blade geometry. In particular, the results show that, for the hovering subsonic conditions considered here, the tonal field is largely governed by the first two non-zero multipoles, which already capture the essential directivity and power content of the tonal field. Once this feature has been established, it becomes useful to seek approximate descriptions of the surface integral to reveal which geometric and aerodynamic mechanisms feed the dominant multipole contributions. To this end, two complementary simplified descriptions are developed. The first is a lifting-surface (LS) formulation, in which the blade is assumed at small incidence. Adopting a thin-airfoil approximation (Ashley *et al.* 1965), the resulting source terms can be decomposed into contributions associated with the pressure jump and the pressure sum over the blades, and the thickness distribution. Because the chordwise phase is retained inside the spanwise integrals, this formulation remains accurate when large-chord effects are important, in particular at higher frequency. The second is a lifting-line (LL) formulation, in which each blade section is assumed compact and collapsed onto a spanwise curve. A local expansion of the Green's function and its gradient is then performed about each radial station, so that the resulting multipole coefficients reduce to one-dimensional spanwise integrals of compact sectional moments. In this case the chordwise phase is neglected, but large incidence and induced-velocity effects are naturally retained. Geometric compactness arguments of this kind have been discussed in several contexts (Hubbard 1991). Here, however, they are exploited within the spherical-multipole framework to clarify the physical content of the leading terms, and in particular to identify how lift, drag, and thickness contribute to the dominant multipoles of the expansion.

To compare the two models on a consistent basis, both sets of multipole coefficients are assessed against exact surface integration on the true blade geometry. This comparison shows that the two approximations perform well in their respective regimes of validity. In particular, once the multipole expansion is truncated to its dominant terms, both approximations retain the relevant acoustic content of the exact solution while yielding substantial computational savings relative to exact surface integration. The theoretical developments are complemented by analyses of far-field directivity, power distribution over harmonics, time-domain waveforms and processing time.

The paper is organized as follows. Section 2 introduces and discusses the spherical-multipole formulation of Goldstein's analogy. Section 3 derives the lifting-surface and lifting-line approx-

imations. Final remarks are given in Section 5. The experimental validation is omitted from the present arXiv version and will be included in the final version of the paper.

2. Multipole Expansion Formulation

Acoustic analogies are exact identities obtained by recasting the compressible-flow equations as a linear wave equation forced by terms that collect the remaining physics (Lighthill 1952, Eq. 4). Their practical use, however, hinges on the crucial assumption to regard the source term as known a priori, even though, there is no exact way to determine the acoustic pressure and the source term independently of one another. In practice, the analogy becomes predictive only under a one-way coupling hypothesis, whereby the flow field is provided by independent calculations or measurements and the acoustic field is computed as the corresponding solution of the linear wave equation. This limitation was recognized from the outset. In Lighthill's original analogy (Lighthill 1952), no solid surfaces were included, and the forcing term was the Lighthill's stress tensor. This tensor involves fluctuating density (or pressure) and therefore contains, in principle, the very unknown of the wave equation. To decouple the forcing from the unknown acoustic field, it was proposed to approximate Lighthill's stress tensor by its Reynolds-stress contribution, which can be estimated from the incompressible part of the flow without explicitly resolving the acoustic component (Goldstein 1976). The validity of this approximation was examined by Crow (1970) through an asymptotic expansion, showing that it is reasonable for sufficiently low Mach numbers and when the characteristic eddy size of the flow is comparable with a representative dimension of the vortical region. The inclusion of solid surfaces as additional source terms is due to the developments of Curle (1955) and Ffowcs Williams & Hawkings (1969). In the context of propeller noise, early studies demonstrated that, at low speeds and for the frequencies relevant to tonal radiation, the Lighthill's contribution is of higher order with respect to the surface ones (Ffowcs Williams & Hawkings 1969) and is therefore commonly neglected in tonal-noise analyses (Hawkings & Lawson 1974).

Under this assumption, in a reference frame where the medium is at rest the acoustic pressure radiated by a moving surface $S(t)$, at source position \mathbf{x} and time t , and observed at position \mathbf{x}_0 and time t_0 , is written as (Goldstein 1976, Eq. 3.6)

$$p(\mathbf{x}_0, t_0) = \int_{-\infty}^{\infty} \int_{S(t)} [\mathbf{f}(\mathbf{x}, t) \cdot \nabla_{\mathbf{x}} G(\mathbf{x}_0, t_0; \mathbf{x}, t) - \rho_0 V_n(\mathbf{x}, t) \partial_t G(\mathbf{x}_0, t_0; \mathbf{x}, t)] dS dt \quad (2.1)$$

where the free-space Green's function (Jackson 1962) is

$$G = \frac{\delta(t_0 - t - |\mathbf{x}_0 - \mathbf{x}|/a_s)}{4\pi|\mathbf{x}_0 - \mathbf{x}|} \quad (2.2)$$

and vector $\mathbf{f}(\mathbf{x}, t)$ is the force per unit area exerted by the body on the fluid and $V_n(\mathbf{x}, t) = \mathbf{V}(\mathbf{x}, t) \cdot \hat{\mathbf{n}}(\mathbf{x}, t)$ is the normal velocity of the surface. We adopt the convention of Hanson & Parzych (1993), in which the unit normal $\hat{\mathbf{n}}$ has outward direction from the blade. In Eq. (2.1), $\nabla_{\mathbf{x}}$ denotes the gradient with respect to the source coordinates, while ∂_t denotes differentiation with respect to the source time. The constants ρ_0 and a_s are the ambient density and speed of sound, respectively.

In the acoustic analogy, the Eq. (2.1) is a closed-form expression to obtain acoustic pressure. This constitutes the key distinction from the classical Kirchhoff-Helmholtz boundary-integral formulation: for the wave equation, the pressure and its normal derivative on a surface cannot be prescribed independently, and their relation is not known a priori, leading to an integral equation to be solved. This overspecification difficulty can be avoided by looking for tailored Green's functions that render one of the boundary conditions unnecessary (Williams 1999; Glegg &

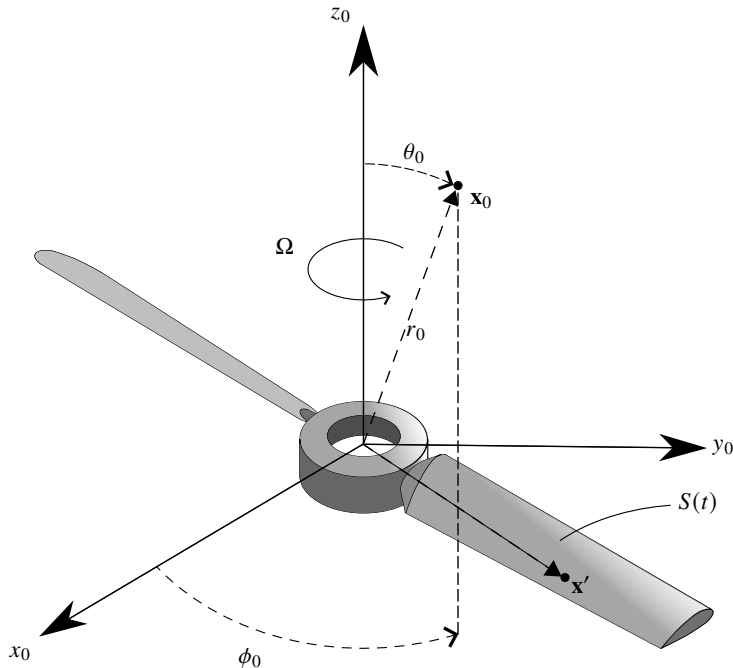


Figure 1: Reference geometry and observer coordinates for the rotating two-bladed propeller. The rotor spins about the z -axis with angular velocity Ω in the fixed Cartesian frame (x, y, z) . The observer is located at \mathbf{x}_0 at distance r_0 from the origin, with spherical elevation (θ_0) and azimuth angles (ϕ_0) . The source position in the frame attached to the propeller is denoted by \mathbf{x}' .

Deavenport 2024). A recent example of this approach, in the context of propeller noise, has been presented by Fruncillo *et al.* (2025).

In the common terminology of aeroacoustics, the source terms $V_n(\mathbf{x}, t)$ and $\mathbf{f}(\mathbf{x}, t)$ in Eq. (2.1) are usually referred to as monopole and dipole. Indeed, those are the far-field behaviours they would exhibit if they were present as isolated point sources. By the same convention, the Lighthill's term neglected here is called a quadrupole. It should be emphasized, however, that this nomenclature pertains only to the local character of an elementary point source: when the radiating surface is observed from distances much larger than its characteristic size, the resulting total field may display complicated features that differ from those of the individual elemental sources. The aim of the present work is precisely to analyze and characterize the far-field multipoles of the radiated sound.

For a propeller rotating at constant angular speed Ω without translation (figure 1), we describe a source point on the blade by $\mathbf{x} = (r, \theta, \phi)$ and the observer position by $\mathbf{x}_0 = (r_0, \theta_0, \phi_0)$, both expressed in spherical coordinates of a fixed inertial frame. Under steady operating conditions, the acoustic pressure measured at a fixed observer location is periodic in time and can therefore be expanded in the Fourier series

$$p(\mathbf{x}_0, t_0) = \sum_{m=-\infty}^{\infty} \hat{p}_m(\mathbf{x}_0) e^{-im\Omega t_0} \quad (2.3)$$

If the rotor consists of N identical blades equally spaced in azimuth, only those harmonics whose index m is an integer multiple of N are non-zero.

It is convenient to evaluate Goldstein's time-domain surface integral, Eq. (2.1), in a frame co-rotating with the blades. In that frame, a source point is described by $\mathbf{x}' = (r', \theta', \phi')$, where

the azimuth ϕ' is fixed to the rotor, and the relation between inertial and rotating coordinates is

$$r = r', \quad \theta = \theta', \quad \phi = \phi' + \Omega t \quad (2.4)$$

Thus, in the rotating frame the blade surface is stationary, and the explicit time dependence associated with the motion of the integration surface can be removed. Following Hanson & Parzych (1993, Eqs. 20 and 28), the harmonic coefficients may then be written as

$$\hat{p}_m(\mathbf{x}_0) = \frac{N}{2\pi} \int_S e^{-im\phi'} \left[\int_0^{2\pi} [\mathbf{f}(\mathbf{x}, \phi) \cdot \nabla_{\mathbf{x}} G_m(\mathbf{x}_0; \mathbf{x}) - i\omega_m \rho_0 V_n(\mathbf{x}, \phi) G_m(\mathbf{x}_0; \mathbf{x})] e^{im\phi} d\phi \right]_{\mathbf{x}=\mathbf{x}'} dS \quad (2.5)$$

where $\omega_m = m\Omega$ is the angular frequency of the m -th harmonic and the time integration has been replaced by an equivalent integration over the inertial azimuth ϕ swept by the source point as the blade rotates. In this expression, the gradient $\nabla_{\mathbf{x}}$ is taken with respect to the source coordinates in the inertial frame, after which the inner integral is evaluated at the source position corresponding to the co-rotating position \mathbf{x}' .

The function

$$G_m(\mathbf{x}_0; \mathbf{x}) = \frac{e^{ik_m|\mathbf{x}_0-\mathbf{x}|}}{4\pi|\mathbf{x}_0-\mathbf{x}|} \quad (2.6)$$

is the free-space Green's function of the Helmholtz equation at wavenumber $k_m = \omega_m/a_s = mk$.

The aim of this work is to achieve a separation between source and observer quantities, so as to obtain a spherical multipole expansion without having to recompute the integrals in Eq. (2.5) each time the observer position is changed. For observers outside the sphere containing the rotor, this can be done through a spherical expansion of the Green's function (Jackson 1962, Eq. 16.22), which we write as

$$G_m(\mathbf{x}_0; \mathbf{x}) = ik_m \sum_{n=-\infty}^{\infty} \sum_{\ell=|n|}^{\infty} f_{\ell n}(\mathbf{x}_0) g_{\ell n}(\mathbf{x}) \quad (2.7)$$

where $f_{\ell n}(\mathbf{x}_0)$ contains all the observer dependence, while $g_{\ell n}(\mathbf{x})$ contains only the source dependence. In particular, in spherical coordinates one has

$$f_{\ell n}(\mathbf{x}_0) = h_{\ell}(k_m r_0) Y_{\ell n}(\theta_0, \phi_0), \quad g_{\ell n}(\mathbf{x}) = j_{\ell}(k_m r) Y_{\ell n}^*(\theta, \phi) \quad (2.8)$$

where h_{ℓ} and $Y_{\ell n}$ are spherical Hankel functions (of the first kind) and spherical harmonics of degree ℓ and order n , whereas j_{ℓ} are spherical Bessel functions and the symbol $*$ indicates complex conjugation.

Under the simplifying assumption that surface fields \mathbf{f} and V_n do not depend explicitly on the azimuth angle ϕ , as is true in hovering conditions, the only explicit dependence on ϕ inside the inner integral is carried by the function $g_{\ell n}(\mathbf{x}) \propto Y_{\ell n}^*(\theta, \phi) \propto e^{-in\phi}$. The inner integration then simply yields

$$\int_0^{2\pi} e^{-i(n-m)\phi} d\phi = 2\pi\delta_{nm} \quad (2.9)$$

where δ_{nm} is the Kronecker delta. The harmonic pressure becomes

$$\hat{p}_m(\mathbf{x}_0) = N i k_m \sum_{\ell=|m|}^{\infty} f_{\ell m}(\mathbf{x}_0) \int_S [\mathbf{f}(\mathbf{x}) \cdot \nabla_{\mathbf{x}} g_{\ell m}(\mathbf{x}) - i\rho_0 a_s k_m V_n(\mathbf{x}) g_{\ell m}(\mathbf{x})]_{\mathbf{x}=\mathbf{x}'} dS \quad (2.10)$$

where the azimuthal dependence $e^{-im\phi'}$ is now contained in the evaluation of function $g_{\ell m}$ in the co-rotating frame. Only the source-dependent functions appear inside the surface integral, while the observer-dependent part $f_{\ell m}(\mathbf{x}_0)$ is factored out. The complex multipole coefficients of

degree ℓ and order m are defined as

$$A_{\ell m} = N i k_m \int_S [\mathbf{f}(\mathbf{x}) \cdot \nabla_{\mathbf{x}} g_{\ell m}(\mathbf{x}) - i \rho_0 a_s k_m V_n(\mathbf{x}) g_{\ell m}(\mathbf{x})]_{\mathbf{x}=\mathbf{x}'} dS \quad (2.11)$$

and depend only on the source geometry and on the surface distributions of $\mathbf{f}(\mathbf{x})$ and $V_n(\mathbf{x})$. The acoustic field at harmonic m can then be written as a spherical multipole expansion in terms of the source coefficients $A_{\ell m}$ as

$$\hat{p}_m(\mathbf{x}_0) = \sum_{\ell=|m|}^{\infty} A_{\ell m} f_{\ell m}(\mathbf{x}_0) \quad (2.12)$$

Once the multipole coefficients $A_{\ell m}$ are known, the acoustic power associated with the harmonic m is proportional to the sum of their squared moduli (Williams 1999, Eq. 6.113), as

$$\Pi_m = \frac{1}{2 \rho_0 a_s k_m^2} \sum_{\ell=|m|}^{\infty} |A_{\ell m}|^2 \quad (2.13)$$

This enables fast, straightforward computations without resorting to far-field pressure integrals, as is otherwise required (Zhong *et al.* 2020).

The surface integral in Eq. (2.11) can be evaluated numerically for an arbitrarily complex blade geometry. The practical advantage of the multipole representation becomes apparent when the expansion in the index ℓ converges rapidly. It is worth noting that, since $\ell \geq |m|$ and the harmonic indices m are integer multiples of the blade count N , the lowest admissible multipole order is constrained by the rotor periodicity. In particular, for $N \geq 2$, that is, excluding the single-blade case, monopole ($\ell = 0$) and dipole ($\ell = 1$) contributions are not admissible; the first possible far-field multipole is therefore at least a quadrupole ($\ell = 2$) for two-bladed propeller.

The complex pressure amplitudes can be obtained from Eq. (2.12) at any observer location lying outside the sphere enclosing the propeller. In propeller acoustics, the emitted frequency content is conveniently expressed in terms of the tip Mach number $M_t = \Omega R / a_s$ where R is the propeller radius, namely the distance between the blade tip and the axis of rotation. Equivalently

$$M_t = kR = \frac{2\pi R}{\lambda} \quad (2.14)$$

where λ is the corresponding wavelength.

In the present work, the main interest is in the radiation observed at large distance from the source, and the analysis therefore focuses primarily on the acoustic far field. In this limit, the spherical representation is especially convenient because the observer-dependent factor $f_{\ell m}(\mathbf{x}_0) = h_{\ell}(m M_t \bar{r}_0) Y_{\ell m}(\theta_0, \phi_0)$ simplifies significantly. For an observer in the far field, the spherical Hankel function admits the large-argument approximation (Jackson 1962, Eq. 16.13)

$$h_{\ell}(m M_t \bar{r}_0) \approx (-i)^{\ell+1} \frac{e^{i m M_t \bar{r}_0}}{m M_t \bar{r}_0}, \quad m M_t \bar{r}_0 \gg \ell \quad (2.15)$$

where $\bar{r}_0 = r_0 / R$ is the observer distance normalized by the propeller radius. Substituting Eq. (2.15) into Eq. (2.12), the complex far-field (FF) pressure coefficient of harmonic m becomes

$$\hat{p}_m^{(FF)}(\mathbf{x}_0) = \frac{e^{i m M_t \bar{r}_0}}{m M_t \bar{r}_0} \sum_{\ell=|m|}^{\infty} (-i)^{\ell+1} A_{\ell m} Y_{\ell m}(\theta_0, \phi_0) \quad (2.16)$$

This expression makes the structure of the far field particularly transparent: the radial decay and propagation are explicit, while the angular dependence is entirely contained in the spherical harmonics, weighted by the multipole coefficients.

2.1. Dominant multipoles

We now examine the multipole coefficients predictions obtained from Eq. (2.11). In particular, we are interested in the decay of the coefficients with respect to the index ℓ , i.e. in the number of terms required to reconstruct the far-field accurately. By contrast, the dependence on the azimuthal index m reflects the frequency content of the radiated field, since each value of m corresponds to a distinct harmonic of the rotor motion (blade-passing frequency, BPF).

To explore these points over a representative range of propeller geometries, two baseline configurations are considered. The choice is also motivated by the developments presented later, since the same configurations will serve as convenient reference cases for discussing the approximate formulations of the surface integral. Propeller A has a relatively large chord-to-diameter ratio $\gamma = c/(2R)$, where c is the local chord length of the blade. For this propeller, $\gamma = 0.20$, and the imposed aerodynamic incidence is $\alpha = 2^\circ$, uniform along the span of the blades. Propeller B has a smaller chord-to-diameter ratio, $\gamma = 0.05$, and a larger incidence, $\alpha = 10^\circ$. Both propellers are two-bladed rotors, so that the blade count is $N = 2$, with tip radius $R = 0.1$ m and hub radius $R_{\text{hub}} = 0.01$ m. The blades are unswept and built with NACA 0012 airfoils along the span. To assess the effect of acoustic compactness, two values of the tip Mach number M_t are considered, namely $M_t = 0.2$ and $M_t = 0.8$. The aerodynamic source terms entering Eq. (2.11) are obtained from sectional aerodynamic data computed with XFOIL (Drela 1989). The calculations are performed at a reference Reynolds number $Re = 10^5$, and at the Mach number corresponding to each operating condition. The imposed angle of attack α is used to obtain the sectional pressure distribution, lift coefficient c_l , and drag coefficient c_d . In addition, the local inflow angle φ_i , associated with the axial induced velocity, is estimated from blade element momentum theory (Bramwell *et al.* 2001; Zhong *et al.* 2020) as

$$N\gamma (c_l - c_d \tan \varphi_i) = 4\pi\bar{r} \sin \varphi_i \tan \varphi_i \quad (2.17)$$

where $\bar{r} = r/R$ is the non-dimensional spanwise coordinate. The resulting local twist distribution is then taken as $\beta(r) = \alpha + \varphi_i(r)$.

A preliminary mesh-convergence study was carried out to identify a discretization yielding grid-independent acoustic predictions. The analysis was carried out for the most demanding case, namely $\gamma = 0.20$ and $M_t = 0.8$, which combines the largest chord ratio with the shortest acoustic wavelength. For this configuration, the full directivity defined by Eq. (B 5) in Appendix B was computed retaining harmonics up to $m = 20$. The discretization was progressively refined until the mean difference, evaluated over the polar angle θ , between successive mesh levels fell below 0.01 dB. The final surface representation employs 34 chordwise points on each side of the airfoil section, for a total of 68 points over the suction and pressure surfaces, with clustering near the leading edge, together with 30 uniformly spaced radial stations between hub and tip. The surface integral in Eq. (2.11) is then evaluated over the corresponding blade surface obtained by connecting the sectional airfoils along the span.

For both propellers and operating conditions, the multipole coefficients have been evaluated for the first harmonics. A first important outcome of these calculations is the very rapid decay of the expansion with respect to the index ℓ . Tables 1-4 show that, for each azimuthal order m , the dominant part of the acoustic field is concentrated in the first two admissible degrees, namely $\ell = m$ and $\ell = m + 1$, while the coefficients associated with $\ell \geq m + 2$ are already much smaller. This means that the leading symmetric ($\ell = m$) and antisymmetric ($\ell = m + 1$) contributions with respect to the rotor plane ($z_0 = 0$) are generally sufficient to capture the essential angular structure of the radiation. The trend is particularly clear at the lower tip Mach number, $M_t = 0.2$. For Propeller A, see table 1, the coefficient at $\ell = m$ is always the largest one, while the next order $\ell = m + 1$ is already smaller by about one order of magnitude. The subsequent terms $\ell = m + 2$ and $\ell = m + 3$ are then reduced by a further one to two orders of magnitude, so that their

$\ell - m $	$m = 2$	$m = 4$	$m = 6$	$m = 8$
0	3.393×10^{-1}	6.863×10^{-2}	8.248×10^{-3}	7.893×10^{-4}
1	4.240×10^{-2}	4.216×10^{-3}	3.188×10^{-4}	2.221×10^{-5}
2	2.992×10^{-4}	1.496×10^{-4}	2.598×10^{-5}	3.031×10^{-6}
3	8.227×10^{-5}	1.633×10^{-5}	1.672×10^{-6}	1.381×10^{-7}

Table 1: Leading multipoles $|A_{\ell m}|$ obtained from Eq. (2.11) for Propeller A at $M_t = 0.2$.

$\ell - m $	$m = 2$	$m = 4$	$m = 6$	$m = 8$
0	6.040×10^{-2}	8.018×10^{-3}	8.344×10^{-4}	7.959×10^{-5}
1	2.668×10^{-2}	2.791×10^{-3}	2.284×10^{-4}	1.738×10^{-5}
2	8.719×10^{-5}	1.939×10^{-5}	2.548×10^{-6}	2.820×10^{-7}
3	5.117×10^{-5}	1.072×10^{-5}	1.194×10^{-6}	1.085×10^{-7}

Table 2: Leading multipoles $|A_{\ell m}|$ obtained from Eq. (2.11) for Propeller B at $M_t = 0.2$.

$\ell - m $	$m = 2$	$m = 4$	$m = 6$	$m = 8$
0	3.160×10^2	8.120×10^2	1.191×10^3	1.358×10^3
1	1.915×10^2	2.625×10^2	2.687×10^2	2.505×10^2
2	4.155	2.460×10^1	5.925×10^1	8.884×10^1
3	6.051	1.708×10^1	2.439×10^1	2.772×10^1

Table 3: Leading multipoles $|A_{\ell m}|$ obtained from Eq. (2.11) for Propeller A at $M_t = 0.8$.

contribution becomes negligible in practice. The same behaviour is observed even more clearly for Propeller B, table 2, where the dominance of the first two multipoles is evident. At the higher tip Mach number, $M_t = 0.8$ in tables 3 and 4, the same hierarchy persists, but the decay becomes less marked. Higher ℓ -orders become more visible, although they still remain distinctly weaker than the first two. A second feature visible in the tables is the behaviour with increasing harmonic index m . At fixed $\ell - m$, the coefficients generally decrease as m increases when $M_t = 0.2$. At $M_t = 0.8$, this decay with m becomes weaker and the coefficients may even grow initially before decreasing at higher frequencies. The dependence on m reflects the frequency content of the subsonic propeller source, a behaviour that is well documented in the experimental literature (Trebble 1987a,b).

To make the previous discussion clearer in angular terms, it is useful to examine the directivity of a single harmonic m while retaining only the first ℓ contributions. For a fixed harmonic index

$\ell - m $	$m = 2$	$m = 4$	$m = 6$	$m = 8$
0	7.146×10^1	1.187×10^2	1.463×10^2	1.621×10^2
1	5.705×10^1	7.849×10^1	8.080×10^1	7.545×10^1
2	1.701	5.221	8.512	1.120×10^1
3	1.793	5.113	7.391	8.465

Table 4: Leading multipoles $|A_{\ell m}|$ obtained from Eq. (2.11) for Propeller B at $M_t = 0.8$.

m , we define the harmonic directivity (see Eq. (B 4) in Appendix B) as

$$D_m(\theta_0, \phi_0) = \frac{4\pi \left| \sum_{\ell=|m|}^{\infty} (-i)^{\ell+1} A_{\ell m} Y_{\ell m}(\theta_0, \phi_0) \right|^2}{\sum_{\ell=|m|}^{\infty} |A_{\ell m}|^2}$$

i.e. the acoustic power radiated per unit solid angle in the direction (θ_0, ϕ_0) , normalized by the total power radiated by that harmonic. For the first non-zero rotor harmonic of the present two-bladed propellers, namely $m = 2$, the first two admissible degrees are $\ell = 2$ and $\ell = 3$. Figure 2 shows the corresponding isolated contributions, their coherent sum, and the complete harmonic directivity reconstructed from the full multipole expansion. From figure 2 emerges that in all four cases the curve obtained by retaining only $\ell = 2$ and $\ell = 3$ is almost indistinguishable from the complete harmonic directivity. This provides direct angular evidence that the first two multipoles already contain essentially all the information needed to reconstruct the exact far-field pattern. Higher ℓ -orders therefore play only a marginal role, even though their coefficients are not identically zero. The two leading multipoles have clearly different angular signatures. The actual directivity is obtained by coherently summing the underlying complex modal amplitudes. The difference between the isolated $\ell = 2$ and $\ell = 3$ contributions and their coherent combination is therefore a direct manifestation of modal interference. In particular, the main lobe of the harmonic directivity is generally displaced toward $\theta_0 > 90^\circ$, and this displacement is reproduced by the coherent sum of the first two multipoles. The direction and magnitude of the shift are thus controlled primarily by the relative amplitude and phase of A_{22} and A_{32} . The relative importance of the two leading multipoles depends on the acoustic compactness, and on the blade geometry and on the operating conditions. At $M_t = 0.2$, especially for Propeller A in panel 2a, the $\ell = 2$ term is clearly dominant and the complete harmonic directivity remains close to its broad single-lobe structure, with only a modest correction induced by $\ell = 3$. In the higher-incidence cases, namely Propeller B at $M_t = 0.2$ in panel 2b and both propellers at $M_t = 0.8$ in panels 2c and 2d, the $\ell = 3$ contribution becomes more important and the interference between $\ell = 2$ and $\ell = 3$ plays a more substantial role in setting the position of the dominant lobe. In general, the first non-zero multipole determines the dominant broad radiation pattern, whereas the second provides the leading off-plane correction. A physical interpretation of the mechanisms contributing to these first two multipoles will be given in the following section, by introducing suitable approximations of the surface integral.

The rapid decay of higher-order ℓ can be understood from the source-side spherical Bessel function j_ℓ , which enters the factor $g_{\ell m}$ in Eq. (2.8). For a given harmonic m , the argument of the spherical Bessel function is $mM_t\bar{r}$. When this quantity is small, the small-argument asymptotics

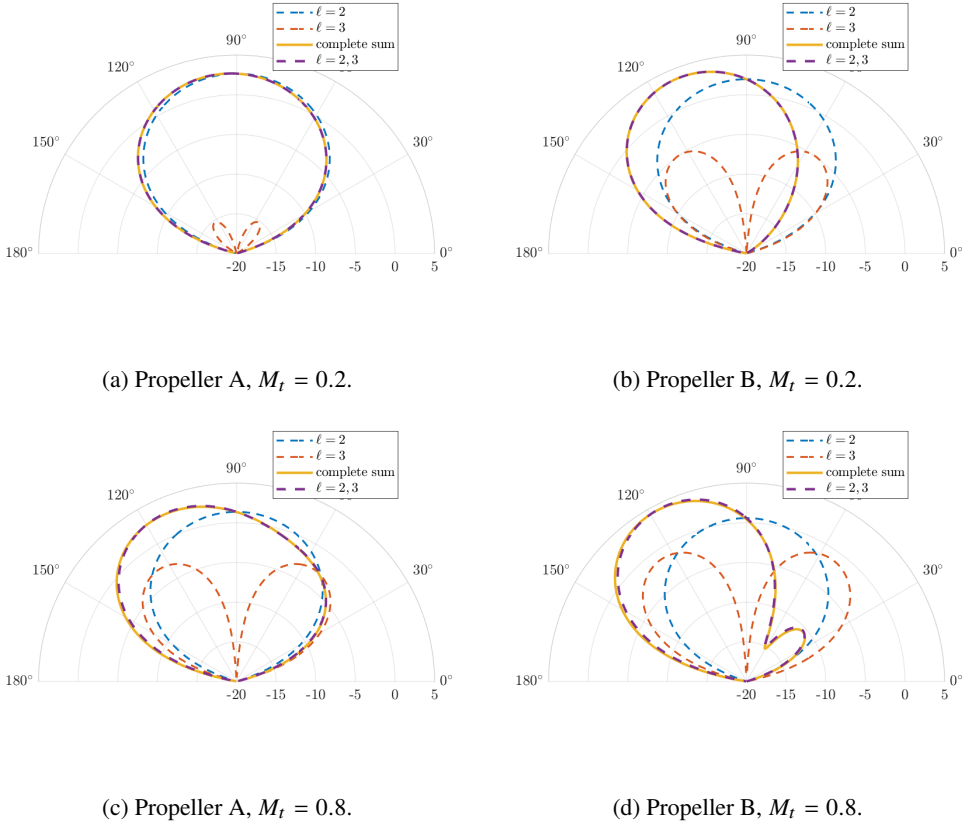


Figure 2: Decomposition of the harmonic directivity for the first non-zero harmonic $m = 2$. The curves show the isolated contributions of the first two degrees, $\ell = 2$ and $\ell = 3$, their coherent sum, and the complete harmonic directivity obtained from the full multipole expansion.

gives (Jackson 1962, Eq. 16.12)

$$j_\ell(mM_t\bar{r}) \approx \frac{(mM_t\bar{r})^\ell}{(2\ell + 1)!!}, \quad mM_t\bar{r} \ll \ell \quad (2.18)$$

This expression shows why large values of ℓ are difficult to excite. Since $\bar{r} \leq 1$, the relevant parameter controlling the excitation of higher multipoles is essentially mM_t . In particular, because the first admissible degree is $\ell = m$, the condition $mM_t\bar{r} \ll \ell$ is satisfied whenever $M_t \ll 1$. It follows that, as the tip Mach number decreases, the higher ℓ -orders are increasingly suppressed and the expansion becomes dominated by the first values of ℓ . This effect on the radiation is especially clear in the far field. Indeed, as far as Eq. (2.16) is concerned, the ℓ -dependence of the solution is governed mainly by the source coefficients $A_{\ell m}$. The attenuation of the higher multipole degrees, inherited from the source-side Bessel function entering those coefficients, is reflected in the far-field behaviour. The mechanism is illustrated in figure 3, which shows the magnitude of $j_\ell(mM_t)$ in the (mM_t, ℓ) -plane. The region $\ell < m$ is excluded because it is not admissible for spherical harmonics of order m . The dotted line corresponds to $\ell = 10mM_t$. Above this line, one is safely in the low-frequency regime $mM_t \ll \ell$, where the Bessel function is already strongly attenuated. This explains why convergence is much faster at $M_t = 0.2$ (panel 3a) than at $M_t = 0.8$ (panel 3b): at lower tip Mach number the admissible multipoles lie deeper inside the attenuated

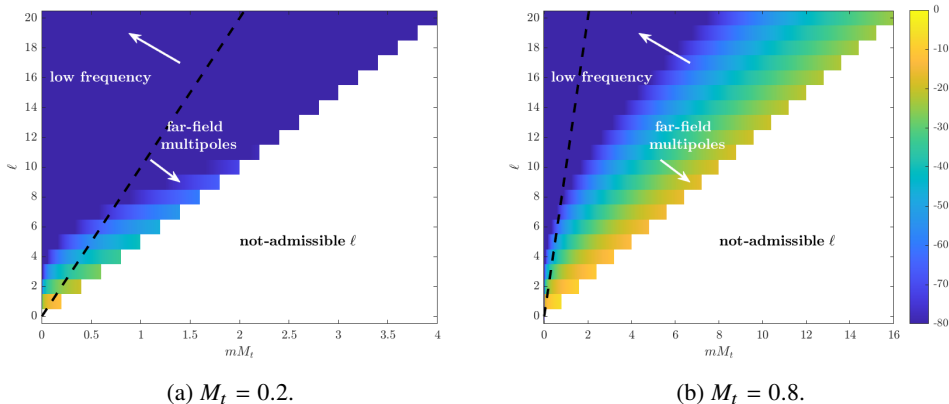


Figure 3: Colour map of $10 \log_{10} |j_\ell(m M_t)|$ [dB] in the $(m M_t, \ell)$ -plane. The region $\ell < m$ is not admissible. The dashed line is $\ell = 10 m M_t$.

region of the map, whereas at higher tip Mach number the first few orders remain closer to the active region and therefore decay more slowly. The same diagram also helps interpret the far-field condition. Since the far-field approximation requires $\ell \ll m M_t \bar{r}_0$, the multipoles lying below the dotted line automatically satisfy this requirement for a distant observer, for example $\bar{r}_0 \approx 100$. In this sense, the region below the dotted curve may be viewed as containing the multipoles that can both be efficiently generated at the source and propagate into the far field for the observer distances considered here.

The rapid decay of the multipole series has an important computational implication. Once the coefficients $A_{\ell m}$ have been computed, the acoustic field at any observer position is obtained by evaluating only the observer-side functions $f_{\ell m}(\mathbf{x}_0)$. The cost of post-processing therefore depends on the number of retained multipoles rather than on repeated blade integrations. As shown previously in Fruncillo *et al.* (2025), this source/observer separation can yield substantial savings with respect to formulations in which the observer dependence remains embedded inside the source integrals (Hanson 1980).

3. Approximations of the Surface Integral

The proposed formulation provides the computation of the multipole coefficients on the surface geometry through Eq. (2.11). However, in that form the physical content of the source remains embedded in a surface integral. Suitable approximations of the geometry are therefore valuable because they make the structure of the acoustic source more explicit. In particular, they can reveal how the different geometric and aerodynamic information enter the leading multipole coefficients, clarifying their symmetry and phase properties, and providing orderings that explain which mechanisms dominate in different operating regimes.

3.1. Lifting surface

In this section we specialise the general expression in Eq. (2.11) to the lifting-surface case. Since the earliest studies of propeller noise (Gutin 1936; Garrick & Watkins 1954), this has been among the most widely adopted modelling approaches. The main benefit is to represent the source field on a geometry that is simpler than the physical one. Here we consider the case in which the reference surface is collapsed onto the equatorial plane, described in rotating coordinates (r, ϕ') at $\theta = \pi/2$. This assumption is commonly used as a starting point, whereby the propeller

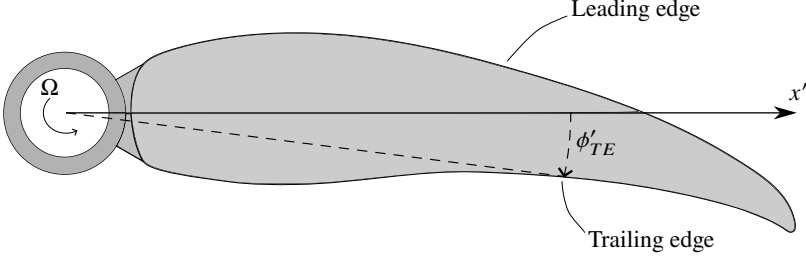


Figure 4: Lifting-surface geometry. The x' -axis is attached to the rotor, passing through the mid-chord of a reference blade section. The trailing-edge position of each section is then described by the azimuthal offset ϕ'_{TE} measured from this line, with counter-clockwise angles taken as positive (negative value in the present example).

surface is approximated by its planform (Carley 1999; Glegg & Devenport 2024). Under this approximation, Eq. (2.11) reduces to

$$A_{\ell m}^{(LS)} = N i k_m \int_{R_{hub}}^R \int_0^{2\pi} [\mathbf{f}(r, \phi') \cdot (\nabla_{\mathbf{x}} g_{\ell m})_0 - i \rho_0 a_s k_m V_n(r, \phi') g_{\ell m, 0}] r dr d\phi' \quad (3.1)$$

where the subscript 0 denotes evaluation on the plane at (r, ϕ') . This approximation is consistent with the classical two-dimensional thin-airfoil theory (Ashley *et al.* 1965). Geometrically, the reference surface lies in the plane of the relative-velocity vector; a small deviation from this plane therefore corresponds to a small aerodynamic incidence too. At a fixed radial station r , the blade section is modelled as a two-dimensional airfoil, whose upper and lower surfaces are described using a dimensionless chordwise coordinate. Although the ϕ' -integration in Eq. (3.1) is written over $[0, 2\pi]$, the integrand is non-zero only over the chordwise extent of the blade at each radius. Denoting by $\phi'_{TE}(r)$ the (co-rotating) azimuth of the trailing edge, as in figure 4), we parametrize the chordwise direction by the coordinate $\xi \in [0, 1]$ as

$$\phi' = \phi'_{TE}(r) + \frac{c(r)}{r} \xi, \quad d\phi' = \frac{c(r)}{r} d\xi \quad (3.2)$$

so that $\xi = 0$ and $\xi = 1$ correspond to the trailing and leading edges, respectively.

Let $z^{(\pm)}(r, \xi)$ denote the normal displacement of the physical blade surface from the equatorial plane, on the upper (+) and lower (-) sides, and define the camber (mean) line and thickness functions as

$$z_{cl} = \frac{z^{(+)} + z^{(-)}}{2}, \quad z_{th} = z^{(+)} - z^{(-)} \quad (3.3)$$

respectively. For a section at small twist angle $\beta(r)$ with respect to the plane of rotation, the upper and lower surfaces can be written as

$$z^{(\pm)}(r, \xi) = z_{cl}(r, \xi) \pm \frac{1}{2} z_{th}(r, \xi) + c(r) \beta(r) \xi \quad (3.4)$$

It is often convenient to normalise by the local chord, writing $z = c h$. This gives the outward (non-unit) normals on the upper and lower surfaces as

$$\mathbf{n}^{(\pm)} = \left(\mp h'_{cl} - \frac{1}{2} h'_{th} \mp \beta \right) \hat{\phi}' \mp \hat{\theta} \quad (3.5)$$

where $h_{cl} = z_{cl}/c$ and $h_{th} = z_{th}/c$, and with symbol ' indicating ξ -differentiation. From the surface geometry we can now obtain the expressions for the force per unit area and for the normal velocity. Retaining only the pressure perturbation contribution to the loading, $\mathbf{f}^{(\pm)} \approx p^{(\pm)} \hat{\mathbf{n}}^{(\pm)}$,

the net force (sum of the contributions from the two sides) can be decomposed in its components along $\hat{\theta}$ and $\hat{\phi}'$ directions as

$$\mathbf{f}_\theta = \Delta p \hat{\theta}, \quad \mathbf{f}_{\phi'} = \left[(\beta + h'_{cl}) \Delta p - \frac{1}{2} h'_{th} \Sigma p \right] \hat{\phi}' \quad (3.6)$$

where $\Delta p = p^{(-)} - p^{(+)}$ is the pressure jump from upper to lower surface and $\Sigma p = p^{(+)} + p^{(-)}$ is their sum.

A similar reduction applies to the normal velocity. From Eq. (3.5) it is easy to see that the only geometric contribution to V_n arises from the thickness distribution, since it has the same sign on both sides, so that

$$V_n = -\Omega \frac{\partial z_{th}}{\partial \phi'} = -\Omega r \frac{\partial h_{th}}{\partial \xi} \quad (3.7)$$

Three physical mechanisms contribute to $A_{\ell m}^{(LS)}$: a normal-loading term \mathbf{f}_θ associated with the pressure jump acting on the plane and whose primary effect is lift when the blade twist is small; a tangential-loading term $\mathbf{f}_{\phi'}$, which involves both the pressure jump and sum and is mainly related to drag; and a thickness term h_{th} , arising from the normal velocity induced by the upper and lower surfaces. Accordingly, each multipole coefficient (ℓ, m) can be expressed in terms of these quantities.

Making explicit the azimuthal dependence of spherical harmonics, $Y_{\ell m}^*(\theta, \phi') = Y_{\ell m}^*(\theta, 0) e^{-im\phi'}$, the function $g_{\ell m}$ and its angular derivatives on the rotor plane are

$$\begin{aligned} g_{\ell m,0} &= j_\ell(k_m r) Y_{\ell m}^*\left(\frac{\pi}{2}, \phi'\right) = j_\ell(k_m r) Y_{\ell m}^*\left(\frac{\pi}{2}, 0\right) e^{-im\phi'} \\ \frac{1}{r} (\partial_\theta g_{\ell m})_0 &= \frac{1}{r} j_\ell(k_m r) \left. \frac{\partial Y_{\ell m}^*}{\partial \theta} \right|_{\theta=\pi/2} = \frac{1}{r} j_\ell(k_m r) \left. \frac{\partial Y_{\ell m}^*(\theta, 0)}{\partial \theta} \right|_{\theta=\pi/2} e^{-im\phi'} \\ \frac{1}{r} (\partial_{\phi'} g_{\ell m})_0 &= \frac{1}{r} j_\ell(k_m r) \left. \frac{\partial Y_{\ell m}^*}{\partial \phi'} \right|_{\theta=\pi/2} = -im \frac{1}{r} j_\ell(k_m r) Y_{\ell m}^*\left(\frac{\pi}{2}, 0\right) e^{-im\phi'} \end{aligned} \quad (3.8)$$

Substituting into Eq. (3.1) yields

$$\begin{aligned} A_{\ell m}^{(LS)} &= N i k_m \int_{R_{hub}}^R j_\ell(k_m r) \frac{c(r)}{r} e^{-im\phi'_{TE}(r)} \int_0^{2\pi} \left[f_L(r, \xi) \left. \frac{\partial Y_{\ell m}^*(\theta, 0)}{\partial \theta} \right|_{\theta=\pi/2} + \right. \\ &\quad \left. - im f_D(r, \xi) Y_{\ell m}^*\left(\frac{\pi}{2}, 0\right) + i \rho_0 a_s k_m \Omega r^2 \frac{\partial h_{th}(r, \xi)}{\partial \xi} Y_{\ell m}^*\left(\frac{\pi}{2}, 0\right) \right] e^{-im \frac{c(r)}{r} \xi} d\xi dr \end{aligned} \quad (3.9)$$

where f_L and f_D are dimensionless pressure coefficients, such that $|\mathbf{f}_\theta| = 1/2\rho_0(\Omega r)^2 f_L$ and $|\mathbf{f}_{\phi'}| = 1/2\rho_0(\Omega r)^2 f_D$. The thickness term in Eq. (3.9) is conveniently rewritten by integrating by parts in ξ , obtaining the equivalent form

$$\begin{aligned} A_{\ell m}^{(LS)} &= N i k_m \int_{R_{hub}}^R j_\ell(k_m r) \frac{c(r)}{r} e^{-im\phi'_{TE}(r)} \int_0^{2\pi} \left[f_L(r, \xi) \left. \frac{\partial Y_{\ell m}^*(\theta, 0)}{\partial \theta} \right|_{\theta=\pi/2} + \right. \\ &\quad \left. - im f_D(r, \xi) Y_{\ell m}^*\left(\frac{\pi}{2}, 0\right) - k_m^2 \rho_0 a_s^2 c(r) r h_{th}(r, \xi) Y_{\ell m}^*\left(\frac{\pi}{2}, 0\right) \right] e^{-im \frac{c(r)}{r} \xi} d\xi dr \end{aligned} \quad (3.10)$$

Rewriting using the non-dimensional radius $\bar{r} = r/R$, the hub ratio $\bar{R}_{hub} = R_{hub}/R$, the chord-to-diameter ratio $\gamma(\bar{r}) = c(\bar{r})/(2R)$, and the tip Mach number $M_t = \Omega R/a_s$, we can collect the

terms and obtain the lifting-surface multipole coefficients as

$$\begin{aligned}
A_{\ell m}^{(LS)} = & i\rho_0 a_s^2 M_t^3 N m B_{L\ell m} \int_{\bar{R}_{hub}}^1 j_\ell(mM_t\bar{r}) \gamma(\bar{r}) \bar{r} e^{-im\phi'_{TE}(\bar{r})} \left[\int_0^1 f_L(\bar{r}, \xi) e^{-im\frac{2\gamma(\bar{r})}{\bar{r}}\xi} d\xi \right] d\bar{r} + \\
& -4i\rho_0 a_s^2 M_t^3 N m^3 B_{T\ell m} \int_{\bar{R}_{hub}}^1 j_\ell(mM_t\bar{r}) \gamma(\bar{r})^2 e^{-im\phi'_{TE}(\bar{r})} \left[\int_0^1 h_{th}(\bar{r}, \xi) e^{-im\frac{2\gamma(\bar{r})}{\bar{r}}\xi} d\xi \right] d\bar{r} + \\
& \rho_0 a_s^2 M_t^3 N m^2 B_{D\ell m} \int_{\bar{R}_{hub}}^1 j_\ell(mM_t\bar{r}) \gamma(\bar{r}) \bar{r} e^{-im\phi'_{TE}(\bar{r})} \left[\int_0^1 f_D(\bar{r}, \xi) e^{-im\frac{2\gamma(\bar{r})}{\bar{r}}\xi} d\xi \right] d\bar{r}
\end{aligned} \tag{3.11}$$

where $B_{L\ell m} = \left. \frac{\partial Y_{\ell m}^*(\theta, 0)}{\partial \theta} \right|_{\theta=\pi/2}$ and $B_{T\ell m} = B_{D\ell m} = Y_{\ell m}^*(\frac{\pi}{2}, 0)$, i.e. they correspond to the values of the spherical harmonics and their θ -derivative evaluated on the equatorial plane $\theta = \pi/2$. These factors encode the angular structure of the radiation and can be written explicitly in terms of ℓ and m , as in the Appendix A. Contributions proportional to $B_{T\ell m}$ are even with respect to $\theta_0 = \pi/2$ (equal modulus above and below the plane) and include thickness and drag; consequently, only terms with $\ell - m$ even survive. Contributions proportional to $B_{L\ell m}$ are odd with respect to $\theta_0 = \pi/2$, yielding an antisymmetric directivity; these arise from lift and therefore involve only terms with $\ell - m$ odd.

This interpretation clarifies which contributions enter the dominant multipole coefficients and explains the directivity patterns discussed in the previous section 2.1. In particular, the lifting-surface approximation adopted here is well suited to propeller A, which operates at low angle of attack. The reason why the low-frequency antisymmetric multipole (Fig. 2a) is so small is that it contains the lift contribution, which remains weaker at small angles of attack than the symmetric contribution, the latter being primarily associated with thickness and drag effects.

3.1.1. Far-field pressure

Once closed-form expressions for the multipole coefficients have been derived, both the acoustic pressure and the radiated sound power can be obtained directly from the general relations Eqs. (2.12) and (2.13). In particular, substituting Eq. (3.11) into Eq. (2.16) yields the complex far-field pressure for the lifting surface

$$\begin{aligned}
\hat{p}_m^{(FF,LS)}(\mathbf{x}_0) \approx & \rho_0 a_s^2 M_t^2 N \frac{e^{imM_t\bar{r}_0}}{\bar{r}_0} \sum_{\ell=|m|}^{\infty} (-i)^\ell Y_{\ell m}(\theta_0, \phi_0) \\
& \left\{ B_{L\ell m} \int_{\bar{R}_{hub}}^1 j_\ell(mM_t\bar{r}) \gamma(\bar{r}) \bar{r} e^{-im\phi'_{TE}(\bar{r})} \left[\int_0^1 f_L(\bar{r}, \xi) e^{-im\frac{2\gamma(\bar{r})}{\bar{r}}\xi} d\xi \right] d\bar{r} + \right. \\
& -4m^2 B_{T\ell m} \int_{\bar{R}_{hub}}^1 j_\ell(mM_t\bar{r}) \gamma(\bar{r})^2 e^{-im\phi'_{TE}(\bar{r})} \left[\int_0^1 h_{th}(\bar{r}, \xi) e^{-im\frac{2\gamma(\bar{r})}{\bar{r}}\xi} d\xi \right] d\bar{r} + \\
& \left. -im B_{D\ell m} \int_{\bar{R}_{hub}}^1 j_\ell(mM_t\bar{r}) \gamma(\bar{r}) \bar{r} e^{-im\phi'_{TE}(\bar{r})} \left[\int_0^1 f_D(\bar{r}, \xi) e^{-im\frac{2\gamma(\bar{r})}{\bar{r}}\xi} d\xi \right] d\bar{r} \right\}
\end{aligned} \tag{3.12}$$

These expressions are equivalent to those obtained by (Hanson 1980, Eq. 36) in his far-field helicoidal-surface theory, when restricted to zero forward velocity. A straightforward comparison can be made and two differences are worth emphasizing. First, in the present formulation each harmonic m is represented through an infinite sum over the index ℓ , whereas Hanson's far-field result are written in closed form. Second, the present multipole expansion introduces spherical

Bessel functions whose argument depends only on the source coordinates and is therefore independent of the observer position. In Hanson’s formulation, by contrast, the corresponding Bessel functions encode the observer location; consequently, the source integrals must be recomputed when the observer position changes. This separation of source and observer is a key practical advantage of the present approach when evaluating pressure at many microphone locations. Moreover, the present framework retains the same formal structure whether or not a far-field assumption is invoked: the pressure is expressed in the same way (but including spherical Hankel functions in the observer factor, instead of the asymptotic limit), and no separate near-field derivation is required. The distinction between near and far field is reflected primarily in the rate of convergence of the truncated series, rather than in a change of the analytical form of the solution. A further advantage concerns the evaluation of radiated power. In Hanson’s formulation the power is typically obtained by an additional integration of the far-field pressure over a control sphere (Zhong *et al.* 2020). In the present multipole approach, instead, the radiated power can be expressed directly in terms of the multipole coefficients by Eq. (2.13), so that its computation reduces to a simple summation.

To understand the phase shift among the three terms, their different symmetry must be taken into account. The lift term is proportional to $(-i)^\ell$, but for fixed m only terms with $\ell - m$ odd contribute; the first non-zero term is therefore $\ell = m + 1$. For the thickness and drag terms, instead, the first contribution is $\ell = m$. Hence, lift $\propto (-i)^{m+1}$, thickness $\propto -(-i)^m$, drag $\propto (-i)^{m+1}$: if the source integrals are real (or if they have approximately the same argument), one obtains that lift and drag are in phase, whereas thickness is in quadrature with them. In the lifting-surface case, however, the phase also contains the contribution of the complex source integrals, and this effect may become significant at higher frequency.

As shown in section 2.1, the first two multipoles are sufficient to obtain an accurate description of the far-field, implying that all three source contributions (lift, drag, and thickness) must in general be retained. Under this condition, the asymptotic form of the spherical harmonics for the lowest degrees at fixed order m is particularly informative. The contributions that are symmetric with respect to the plane of rotation (e.g., thickness and drag) are associated with the first non-zero sectoral term $Y_{mm}(\theta_0, \phi_0) \propto (\sin \theta_0)^m e^{im\phi_0}$ (Khersonskii *et al.* 1988, p. 157, Eq. 12). In contrast, an antisymmetric contribution (e.g., lift) requires a factor that changes sign across the plane, and is captured by $Y_{m+1,m}(\theta_0, \phi_0) \propto \cos \theta_0 (\sin \theta_0)^m e^{im\phi_0}$ (Khersonskii *et al.* 1988, p. 157, Eq. 13). These expressions allow straightforward considerations about the directivity of a single m -harmonic, as will be discussed later.

3.2. Lifting line

The approach developed in the previous section 3.1 is well suited to propellers whose blades are moderately twisted and operate at small incidence. Many practical propellers, however, feature large inflow angles and high-aspect-ratio blades. In this section we therefore specialise Goldstein’s integral to the case of slender blades operating at arbitrary incidence. The blade is approximated by a spanwise lifting curve, along which compact airfoil sections are distributed.

Fix a station point $\mathbf{x}'_s(\lambda)$ in the frame co-rotating with the lifting curve, with radius $r_s = |\mathbf{x}_s| \in [R_{\text{hub}}, R]$. Let $2R$ be the outer scale and c the inner scale, and introduce the small parameter $\varepsilon_\ell = c/(2R) = \gamma \ll 1$. A small sectional patch around \mathbf{x}'_s is parametrised by a local coordinate ξ in the airfoil section as

$$\mathbf{x}'(\lambda, \mu; \varepsilon_\ell) = \mathbf{x}'_s(\lambda) + \varepsilon_\ell \xi(\lambda, \mu) \quad (3.13)$$

where λ is a spanwise coordinate and μ parametrises the closed section contour. The full blade surface is swept out by moving these closed sectional curves along the span. From an aerodynamic viewpoint, see figure 5, it is natural to assume that the local sections remain aligned with the incoming relative flow, so that the radial coordinate provides the most convenient spanwise

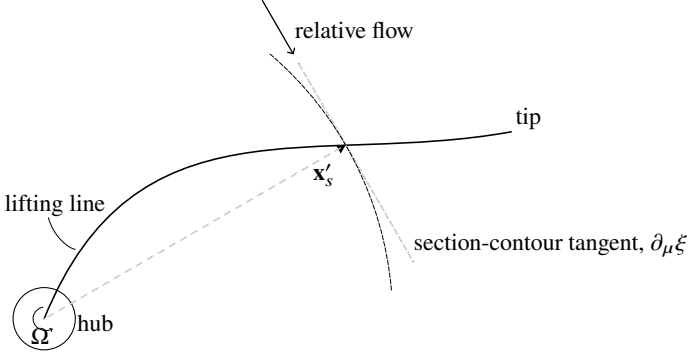


Figure 5: Lifting-line geometry.

parametrisation. Accordingly, in what follows we take $\lambda = r$. If the blade surface is viewed as the surface generated by intersecting the blade with spheres centred at the hub, and if $dl = |\partial_\mu \xi(\lambda, \mu)| d\mu$ denotes the arc-length element of the section contour, then the surface element is simply written as $dS = \varepsilon_\ell dl dr$. With this choice, the original surface integral can be reduced to a contour integral over each compact section followed by a spanwise integration along the lifting line.

The acoustic function $g_{\ell m}$ can be expanded around the station point \mathbf{x}'_s as

$$\begin{aligned} g_{\ell m}(\mathbf{x}) &= g_{\ell m,s} + \varepsilon_\ell \xi \cdot \nabla_s g_{\ell m,s} + O(\varepsilon_\ell^2) \\ \nabla_{\mathbf{x}} g_{\ell m}(\mathbf{x}) &= \nabla_s g_{\ell m,s} + \varepsilon_\ell (\nabla_s \nabla_s g_{\ell m,s}) \cdot \xi + O(\varepsilon_\ell^2) \end{aligned} \quad (3.14)$$

where the subscript s denotes evaluation at \mathbf{x}'_s and ∇_s acts on the source coordinates. The Taylor expansion is applied only to $g_{\ell m}$ and its gradient whereas the sources \mathbf{f} and V_n are kept in their exact form.

Substituting Eq. (3.14) into Eq. (2.11), the multipole coefficient $A_{\ell m}^{(LL)}$ for the lifting line becomes

$$\begin{aligned} A_{\ell m}^{(LL)} &\approx N i k_m \int_{R_{hub}}^R \left\{ \varepsilon_\ell \oint_{\partial S} \left[\underbrace{\mathbf{f} \cdot \nabla_s g_{\ell m,s}}_{\text{force term}} - \underbrace{i k_m \rho_0 a_s V_n g_{\ell m,s}}_{\text{velocity term}} \right] dl + \right. \\ &\quad \left. + \varepsilon_\ell^2 \oint_{\partial S} \left[\underbrace{\mathbf{f} \cdot (\nabla_s \nabla_s g_{\ell m,s}) \xi}_{\text{force moment}} - \underbrace{i k_m \rho_0 a_s V_n \xi \cdot \nabla_s g_{\ell m,s}}_{\text{velocity moment}} \right] dl \right\} dr \end{aligned} \quad (3.15)$$

We then define the compact force and velocity moments over ∂S as

$$\begin{aligned} \mathbf{F}_s &= \oint_{\partial S} \mathbf{f} dl, & Q_{V,s} &= \oint_{\partial S} V_n dl, \\ \mathbf{M}_s^{(f)} &= \oint_{\partial S} \mathbf{f} \otimes \xi dl, & \mathbf{M}_s^{(V)} &= \oint_{\partial S} V_n \xi dl \end{aligned} \quad (3.16)$$

Here \mathbf{F}_s is the resultant sectional force (per unit length, acting on the fluid), $Q_{V,s}$ is the net normal volume flux through the sectional patch, $\mathbf{M}_s^{(f)}$ is the first moment of the force, and $\mathbf{M}_s^{(V)}$ is the

first moment of the normal velocity. Using these definitions we obtain the compact expression

$$A_{\ell m}^{(LL)} \approx N i k_m \int_{R_{hub}}^R \left[\varepsilon_{\ell} \left(\mathbf{F}_s \cdot \nabla_s g_{\ell m, s} - i k_m \rho_0 a_s Q_{V, s} g_{\ell m, s} \right) + \varepsilon_{\ell}^2 \left(\mathbf{M}_s^{(f)} : \nabla_s \nabla_s g_{\ell m, s} - i k_m \rho_0 a_s \mathbf{M}_s^{(V)} \cdot \nabla_s g_{\ell m, s} \right) \right] dr \quad (3.17)$$

At first order, the expansion yields two terms. For an impermeable blade section, the velocity term $Q_{V, s}$ vanishes by local mass conservation, so that the first non-zero contribution is force-related \mathbf{F}_s , in agreement with the analysis of Brouwer (1989). To better understand the sectional force, it is convenient to decompose \mathbf{f} into a component normal to the airfoil section ($(\mathbf{f} \cdot \hat{\mathbf{x}}_s) \hat{\mathbf{x}}_s$) and a component lying within the section plane (\mathbf{f}_{\perp})

$$\mathbf{f} = (\mathbf{f} \cdot \hat{\mathbf{x}}_s) \hat{\mathbf{x}}_s + \mathbf{f}_{\perp}, \quad \mathbf{f}_{\perp} = \mathbf{f} - (\mathbf{f} \cdot \hat{\mathbf{x}}_s) \hat{\mathbf{x}}_s \quad (3.18)$$

The corresponding scalar and vector moments over the sectional patch ∂S are

$$F_r = \oint_{\partial S} (\mathbf{f} \cdot \hat{\mathbf{x}}_s) dl, \quad \mathbf{F}_{\perp} = \oint_{\partial S} \mathbf{f}_{\perp} dl, \quad (3.19)$$

$$\mathbf{I}_{\perp}^{(f)} = \oint_{\partial S} \xi (\mathbf{f} \cdot \hat{\mathbf{x}}_s) dl, \quad \mathbf{M}_{\perp}^{(f)} = \oint_{\partial S} \mathbf{f}_{\perp} \otimes \xi dl$$

Here F_r and \mathbf{F}_{\perp} are the radial and in-plane components of the resultant sectional force. The quantities $\mathbf{I}_{\perp}^{(f)}$ and $\mathbf{M}_{\perp}^{(f)}$ are the first moments of the radial and in-plane force components. In terms of these sectional moments, the compact force moments in Eq. (3.17) can be written as

$$\mathbf{F}_s = F_r \hat{\mathbf{x}}_s + \mathbf{F}_{\perp}, \quad \mathbf{M}_s^{(f)} = \hat{\mathbf{x}}_s \otimes \mathbf{I}_{\perp}^{(f)} + \mathbf{M}_{\perp}^{(f)} \quad (3.20)$$

The in-plane tensor $\mathbf{M}_{\perp}^{(f)}$ contains the first moments of the in-plane force about axes in the section plane. It is useful to distinguish the symmetric and skew-symmetric parts of $\mathbf{M}_{\perp}^{(f)}$. The skew-symmetric part $\mathbf{M}_{\perp}^{(f), \text{skew}}$ is directly related to the classical aerodynamic moment of the airfoil section about the radial axis. Indeed the scalar pitching moment about $\hat{\mathbf{x}}_s$ is

$$M_{\text{pitch}} = \oint_{\partial S} (\xi \times \mathbf{f}_{\perp}) \cdot \hat{\mathbf{x}}_s dl \quad (3.21)$$

which can be expressed in terms of $\mathbf{M}_{\perp}^{(f), \text{skew}}$. However, because the Hessian $\nabla_s \nabla_s g_{\ell m, s}$ is symmetric, only the symmetric part $\mathbf{M}_{\perp}^{(f), \text{sym}}$ contributes to the acoustic term $\mathbf{M}_s^{(f)} : \nabla_s \nabla_s g_{\ell m, s}$ in Eq. (3.17). The skew-symmetric part, and hence the classical sectional pitching moment, does not enter the solution at the order considered here.

3.2.1. Straight line in the equatorial plane

The general expressions above can be simplified further for geometries representative of many practical propellers. Away from the hub and tip regions where three-dimensional effects are strongest, the local aerodynamic loading is approximately two-dimensional (Johnson 2013). The resultant sectional force is then dominated by the lift and drag components acting in the local airfoil plane, denoted by \mathbf{L}_s and \mathbf{D}_s (forces per unit span exerted on the fluid), whereas the radial component may be neglected. Accordingly, all moments associated with the radial force become negligible; in particular $F_r \approx 0$ and $\mathbf{I}_{\perp}^{(f)} \approx \mathbf{0}$.

As discussed by Brouwer (1992), a thin-airfoil assumption is not strictly required in a lifting-line formulation, but it is convenient when seeking a simpler description. In particular, if the

airfoil is small enough to consider normal velocity uniform over the section, then the first moment of the velocity may be approximated as

$$\mathbf{M}_s^{(V)} = \oint_{\partial S} (\mathbf{V} \cdot \mathbf{n}) \boldsymbol{\xi} dl \approx \mathbf{u}_s \cdot \oint_{\partial S} \mathbf{n} \otimes \boldsymbol{\xi} dl = A_s \mathbf{u}_s \quad (3.22)$$

where \mathbf{u}_s is the section velocity and A_s is the section area.

Moreover, for a generic airfoil the symmetric force-moment tensor $\mathbf{M}_\perp^{(f),\text{sym}}$ should be regarded as being of the same order as the first moment of the velocity $\mathbf{M}_s^{(V)}$, according to Eq. (3.17). Under a thin-airfoil approximation, however, the leading symmetric part depends only on the first moment of the pressure jump Δp about the chosen sectional reference point. If that point is taken sufficiently close to the center of pressure, this leading-order symmetric contribution vanishes. Under these assumptions, the dominant sectional moments reduce to the resultant lift-drag force and to the area-related velocity moment

$$\mathbf{F}_s \approx \mathbf{F}_\perp \approx \mathbf{L}_s + \mathbf{D}_s, \quad Q_{V,s} \approx 0, \quad \mathbf{M}_s^{(f)} \approx \mathbf{M}_\perp^{(f),\text{sym}} \approx 0, \quad \mathbf{M}_s^{(V)} \approx A_s \mathbf{u}_s \quad (3.23)$$

Substituting Eqs. (3.23) in Eq. (3.17) then gives

$$A_{\ell m}^{(LL)} = N i k_m \int_{R_{hub}}^R \frac{j_\ell(k_m r)}{r} \nabla_{\Omega_s} Y_{\ell m}^*(\hat{\mathbf{x}}_s) \cdot [\varepsilon_\ell(\mathbf{L}_\perp(r) + \mathbf{D}_\perp(r)) - \varepsilon_\ell^2 i \omega_m \rho_0 \mathbf{u}_s(r) A_s(r)] dr \quad (3.24)$$

where ∇_{Ω_s} denotes the angular gradient with respect to the source coordinates. To facilitate comparison with the lifting-surface results, we now restrict attention to the case in which the lifting line lies in the equatorial plane, $\theta = \pi/2$. In this case

$$\nabla_{\Omega_s} Y_{\ell m}^*(\hat{\mathbf{x}}_s) = \left. \frac{\partial Y_{\ell m}^*(\theta, 0)}{\partial \theta} \right|_{\theta=\pi/2} e^{-im\phi'_s} \hat{\boldsymbol{\theta}} - im Y_{\ell m}^*\left(\frac{\pi}{2}, 0\right) e^{-im\phi'_s} \hat{\boldsymbol{\phi}}' \quad (3.25)$$

with ϕ'_s denoting the azimuthal position of the lifting line.

The lifting-line approach allows the local induced velocity (Bramwell *et al.* 2001) to be taken into account. Defining φ_i as the inflow angle, namely the angle between the rotor plane and the local relative velocity vector, the magnitude of the local relative velocity is given by

$$|\mathbf{u}_s| = \frac{\Omega r}{\cos \varphi_i} \quad (3.26)$$

The sectional lift and drag are then written as $\mathbf{L}_s + \mathbf{D}_s = q_s c \left(c_l \hat{\mathbf{L}} + c_d \hat{\mathbf{D}} \right)$, where

$$\hat{\mathbf{L}} = \cos \varphi_i \hat{\boldsymbol{\theta}} + \sin \varphi_i \hat{\boldsymbol{\phi}}', \quad \hat{\mathbf{D}} = \hat{\mathbf{u}}_s = -\sin \varphi_i \hat{\boldsymbol{\theta}} + \cos \varphi_i \hat{\boldsymbol{\phi}}' \quad (3.27)$$

and $q_s = \frac{1}{2} \rho_0 \Omega^2 r^2 / \cos^2 \varphi_i$ is the local dynamic pressure.

Substituting these expressions into Eq. (3.24) yields the first-order multipole coefficients

$$\begin{aligned} A_{\ell m}^{(LL,1)} &= i \rho_0 a_s^2 m M_t^3 N B_{L\ell m} \int_{\bar{R}_{hub}}^1 j_\ell(m M_t \bar{r}) \frac{\gamma(\bar{r})}{\cos \varphi_i(\bar{r})} [c_l(\bar{r}) - c_d(\bar{r}) \tan \varphi_i(\bar{r})] \bar{r} e^{-im\phi_s(\bar{r})} d\bar{r} + \\ &+ \rho_0 a_s^2 m^2 M_t^3 N B_{D\ell m} \int_{\bar{R}_{hub}}^1 j_\ell(m M_t \bar{r}) \frac{\gamma(\bar{r})}{\cos \varphi_i(\bar{r})} [c_l(\bar{r}) \tan \varphi_i(\bar{r}) + c_d(\bar{r})] \bar{r} e^{-im\phi_s(\bar{r})} d\bar{r} \end{aligned} \quad (3.28)$$

and the second-order multipole coefficients

$$\begin{aligned}
 A_{\ell m}^{(LL,2)} = & -4i\rho_0 a_s^2 m^3 M_t^3 N B_{T_{\ell m}} \int_{\bar{R}_{hub}}^1 j_\ell(m M_t \bar{r}) \gamma^2(\bar{r}) A_s(\bar{r}) e^{-im\phi_s(\bar{r})} d\bar{r} + \\
 & -4\rho_0 a_s^2 m^2 M_t^3 N B_{T'_{\ell m}} \int_{\bar{R}_{hub}}^1 j_\ell(m M_t \bar{r}) \gamma^2(\bar{r}) A_s(\bar{r}) \tan \varphi_i(\bar{r}) e^{-im\phi_s(\bar{r})} d\bar{r}
 \end{aligned} \tag{3.29}$$

As in the lifting-surface case, symmetry with respect to the plane of rotation remains embedded in the factors $B_{L_{\ell m}} = B_{T'_{\ell m}}$ and $B_{D_{\ell m}} = B_{T_{\ell m}}$. The leading-order term is governed by sectional lift and drag, both of which scale with the slenderness parameter $\varepsilon_\ell = \gamma$, whereas the thickness-related corrections enter only at order γ^2 . To facilitate comparison with the lifting-surface formulation, the two terms in Eq. (3.28) are referred to here as the ‘‘lift’’ and ‘‘drag’’ contributions. In the lifting-line framework, however, these terms are not associated exactly with directions normal and tangential to the plane of rotation. As a result, the first term may also contain a non-negligible drag-related contribution, just as the second may include a lift-related component. The first term in Eq. (3.29) is clearly related to the sectional area and is therefore again denoted as the ‘‘thickness’’ contribution. The last term is referred to as ‘‘induced thickness’’, since it vanishes in the absence of induced velocity. The lifting-line approximation therefore captures the aerodynamic effects associated with large incidence and induced velocity, while the thickness contribution is a higher-order correction in the slender-blade parameter.

This interpretation also helps explain the directivity patterns discussed in Section 2.1. In particular, the lifting-line approximation adopted here is well suited to propeller B, which operates at a higher angle of attack. The prominence of the antisymmetric multipoles (Figs. 2b and 2d) can be attributed to the fact that they contain the lift contribution, which is comparatively stronger in this case.

The inflow angle introduces an additional correction in the ε -scaling. Using the Eq. (3.30) from blade element momentum theory and considering the hovering limit $\varphi_i \ll 1$, in which $(c_l - c_d \tan \varphi_i) \approx c_l$ is reasonable, it follows that

$$\varphi_i \approx \sqrt{\frac{N c_l \gamma}{4\pi \bar{r}}} = \sqrt{\frac{N c_l}{4\pi \bar{r}}} \sqrt{\varepsilon_\ell} \tag{3.30}$$

so that, in this regime, the inflow angle scales as $\varphi_i = O(\varepsilon_\ell^{1/2})$. If the spanwise integration in Eqs. (3.28) and (3.29) does not modify the ε_ℓ -order, then the four contributions in Eqs. (3.28) and (3.29) scale as

$$\begin{aligned}
 \text{lift term} & \sim O(\varepsilon_\ell) + O\left(\varepsilon_\ell^{3/2}/E\right) \\
 \text{drag term} & \sim O\left(\varepsilon_\ell^{3/2}\right) + O(\varepsilon_\ell/E) \\
 \text{thickness term} & \sim O\left(\varepsilon_\ell^2\right) \\
 \text{induced-thickness term} & \sim O\left(\varepsilon_\ell^{5/2}\right)
 \end{aligned}$$

where $E = c_l/c_d$ is the aerodynamic efficiency of the airfoil. The leading lift contribution is therefore $O(\varepsilon_\ell)$, while the drag contribution is reduced either by small inflow angle or by high efficiency. Thickness enters only at the next order, $O(\varepsilon_\ell^2)$, and the induced-thickness correction is smaller still.

3.2.2. Far-field pressure

Far-field expressions can be found by using substituting Eqs. (3.28) and (3.29) in Eq. (2.16), yielding

$$\begin{aligned}
 \hat{p}_m^{(FF,LL)}(\mathbf{x}_0) \approx & \rho_0 a_s^2 M_t^2 N \frac{e^{imM_t\bar{r}_0}}{\bar{r}_0} \sum_{\ell=|m|}^{\infty} (-i)^\ell Y_{\ell m}(\theta_0, \phi_0) \\
 & \left\{ B_{L_{\ell m}} \int_{\bar{R}_{hub}}^1 j_\ell(mM_t\bar{r}) \frac{\gamma(\bar{r})}{\cos \varphi_i(\bar{r})} [c_l(\bar{r}) - c_d(\bar{r}) \tan \varphi_i(\bar{r})] \bar{r} e^{-im\phi_s(\bar{r})} d\bar{r} + \right. \\
 & -imB_{D_{\ell m}} \int_{\bar{R}_{hub}}^1 j_\ell(mM_t\bar{r}) \frac{\gamma(\bar{r})}{\cos \varphi_i(\bar{r})} [c_l(\bar{r}) \tan \varphi_i(\bar{r}) + c_d(\bar{r})] \bar{r} e^{-im\phi_s(\bar{r})} d\bar{r} + \\
 & -4m^2 B_{T_{\ell m}} \int_{\bar{R}_{hub}}^1 j_\ell(mM_t\bar{r}) \gamma(\bar{r})^2 A_s(\bar{r}) e^{-im\phi'_s(\bar{r})} d\bar{r} + \\
 & \left. +4imB_{T'_{\ell m}} \int_{\bar{R}_{hub}}^1 j_\ell(mM_t\bar{r}) \gamma(\bar{r})^2 A_s(\bar{r}) \tan \varphi_i(\bar{r}) e^{-im\phi'_s(\bar{r})} d\bar{r} \right\} \quad (3.31)
 \end{aligned}$$

The phase structure follows the same symmetry argument discussed for the lifting-surface formulation, but is somewhat simpler here because no additional chordwise phase factor is present. The lift and drag terms are associated with the leading antisymmetric and symmetric multipoles, respectively, and their prefactors combine so that, when the spanwise integrals are real or have comparable arguments, the two contributions are approximately in phase. The thickness term, by contrast, carries an additional factor that places it in quadrature with lift and drag at leading order. The induced-thickness correction is a quadrature term too, since it enters through the antisymmetric poles. More generally, the total phase of each contribution also contains the argument of the azimuth position, through the factor $e^{-im\phi_s(\bar{r})}$; thus, the above phase relations should be interpreted as the baseline structure, upon which the spanwise source distribution introduces additional corrections.

As before, the lowest admissible multipoles are the most informative. Symmetric contributions ($\ell = m$), such as drag and the leading thickness term, are associated with the first non-zero sectoral harmonic Y_{mm} , whereas antisymmetric contributions ($\ell = m + 1$), such as lift and induced thickness, first appear through $Y_{m+1,m}$.

3.3. Comparison with exact integration

In this section we discuss the results obtained from the presented approximations. First, the predictions obtained with the lifting-surface and lifting-line formulations are compared against the “exact” prediction of Eq. (2.11), i.e. based on the surface integral evaluated on the true blade geometry. The purpose of this comparison is to assess when the two approximations are applicable and to quantify their accuracy over representative operating conditions. The same propellers A and B introduced in section 2.1 are considered here. As expected, the lifting-surface (LS) formulation should perform better for propeller A, whereas the lifting-line (LL) formulation is anticipated to be more suitable for propeller B. Since both propellers are unswept, the trailing-edge azimuthal phase is taken as $\phi'_{TE} = c/(2r)$ for the LS model, while $\phi'_s = 0$ is adopted for the LL model, implying that the lifting line passes through the mid-chord line of each airfoil section.

For clarity, the main acoustic quantities reported in the figures are defined in the Appendix B. A quantity of particular interest in the present framework is the total directivity of the radiated

pressure field

$$D(\theta_0, \phi_0) = \frac{4\pi \sum_{m=-\infty}^{\infty} \frac{1}{m^2} \left| \sum_{\ell=|m|}^{\infty} (-i)^{\ell+1} A_{\ell m} Y_{\ell m}(\theta_0, \phi_0) \right|^2}{\sum_{m=-\infty}^{\infty} \frac{1}{m^2} \sum_{\ell=|m|}^{\infty} |A_{\ell m}|^2}$$

It measures the acoustic radiation in a given direction relative to its spherical average. It is frequently expressed in dB so that directions with $D(\theta_0, \phi_0) \geq 0$ dB correspond to above-average radiation, whereas directions with $D < 0$ dB identify weakly radiating regions.

Figure 6 shows that both reduced models reproduce the main features of the radiation pattern with generally good accuracy, while also highlighting the expected differences in their respective ranges of validity. Overall, the lifting-surface (LS) approximation provides the closest agreement with the exact solution. This is especially evident for Propeller A, which corresponds to the larger-chord, low-incidence configuration and therefore matches more closely the assumptions underlying the LS formulation. At the same time, the results for Propeller B indicate that the lifting-line (LL) approximation performs noticeably better there than it does for Propeller A, consistently with the smaller chord and higher incidence of that propeller. For Propeller A at $M_t = 0.2$ (panel 6a), both approximations are in very close agreement with the exact solution. The main lobe is nearly symmetric about the rotor plane, and both reduced models accurately reproduce its orientation, width, and peak level. In this low-Mach-number condition, the first few harmonics dominate and finite-chord phase effects remain weak, so that both simplified descriptions provide an adequate representation of the source. At the higher tip Mach number $M_t = 0.8$ (panel 6c), the difference between the two approximations becomes more evident. The LS solution remains close to the exact one, correctly reproducing both the overall lobe shape and the slight displacement of the maximum away from $\theta_0 = 90^\circ$. By contrast, the LL model predicts a stronger peak located too close to the rotor plane. This behaviour is consistent with the fact that, as M_t increases, higher harmonics become more relevant and chordwise phase effects play a more visible role. For Propeller B at $M_t = 0.2$ (panel 6b), both reduced models again provide a good approximation of the exact directivity, including the tilted main lobe and the overall fore-aft asymmetry. A similar conclusion holds for Propeller B at $M_t = 0.8$ (panel 6d): the LS formulation remains almost indistinguishable from the exact solution, while the LL model also performs well and captures the global pattern with only small residual differences. In particular, LL prediction is noticeably closer to the exact solution than it was for Propeller A at the same Mach number, since the relatively small chord of Propeller B makes the compact LL representation more reliable than in the large-chord configuration. Overall, Fig. 6 confirms that the approximations provide accurate description of the directivity in their respective regime of validity. At the same time, the results show that LS is the more robust approximation over the range of cases considered here, whereas LL becomes increasingly competitive as the blade geometry and loading approach the slender, higher-incidence regime for which it is intended.

The rapid convergence of the multipole series discussed in section 2.1 allows, at least in the low-frequency regime, to understand the location of the dominant directivity lobe directly from the first two admissible multipoles. If the acoustic field is dominated by the first non-zero rotor harmonic $m = N$, and only the leading terms $\ell = N$ and $\ell = N + 1$ are retained, then the directivity reduces to

$$D(\theta_0, \phi_0) \propto \left| (-i)^{N+1} A_{NN} Y_{NN}(\theta_0, \phi_0) + (-i)^{N+2} A_{N+1,N} Y_{N+1,N}(\theta_0, \phi_0) \right|^2 \quad (3.32)$$

At low frequency, using the small-argument approximation of the spherical Bessel functions, Eq.

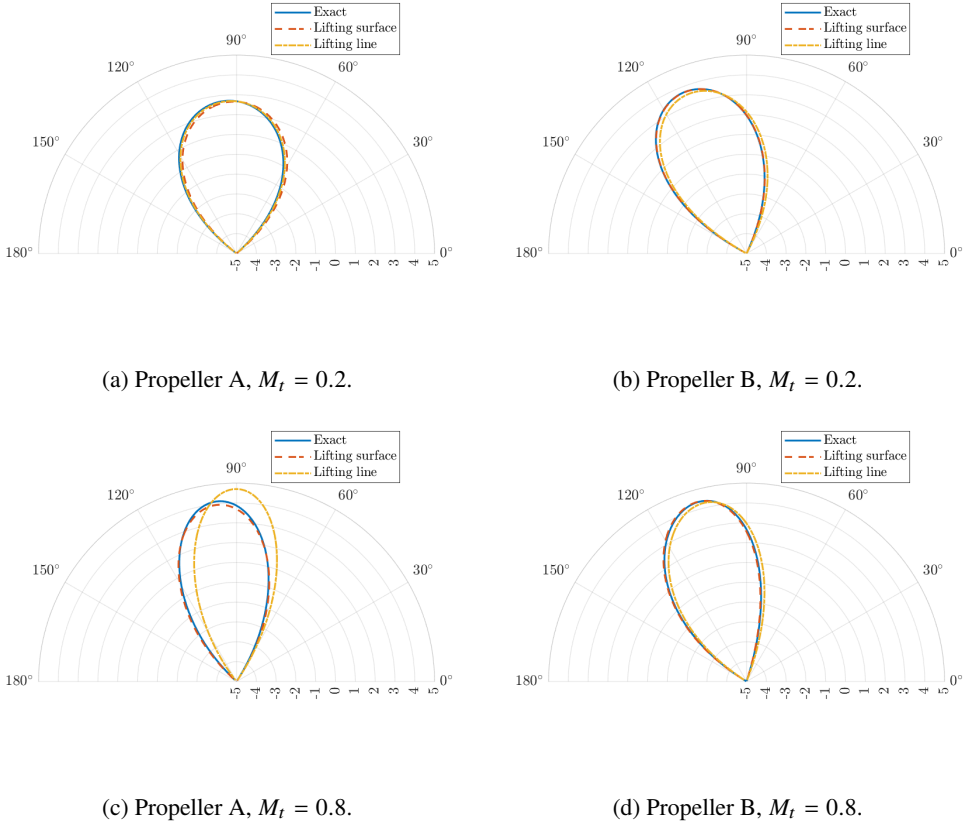


Figure 6: Directivity D [dB] for the exact solution and the lifting-surface/line approximations.

(2.18), one finds that

$$A_{NN} = O(M_t^{N+3}), \quad A_{N+1,N} = O(M_t^{N+4})$$

Therefore, the antisymmetric contribution associated with $(\ell, m) = (N + 1, N)$ is smaller by one additional power of M_t than the symmetric one associated with $(\ell, m) = (N, N)$. This implies that, in the low-frequency limit, the directivity is primarily governed by the symmetric component, while the antisymmetric correction becomes progressively important only as M_t increases, or when the lift contribution (that is captured by antisymmetric poles) is sufficiently strong. It is also worth noting that, since both retained harmonics share the same azimuthal factor $e^{iN\phi_0}$, this dependence cancels out upon taking the modulus squared. As a result, the directivity depends only on θ_0 .

The harmonic power spectra in Fig. 7 provide a complementary assessment of the accuracy of the two approximate models, since they reveal the rate at which the acoustic energy decays in frequency. At the lower tip Mach number, shown in panels 7a and 7b, both approximations reproduce the low-pass character of the spectrum well. In agreement with experimental evidence (Treble 1987a,b), the radiated power decreases rapidly with increasing m , so that the acoustic output is dominated by the first few blade-passing harmonics. In this regime, the LS and LL predictions are both very close to the exact solution over the dominant low-order harmonics. For Propeller B at $M_t = 0.2$, the agreement remains excellent over the whole range shown, whereas for Propeller A at $M_t = 0.2$ the LL approximation begins to overpredict the highest

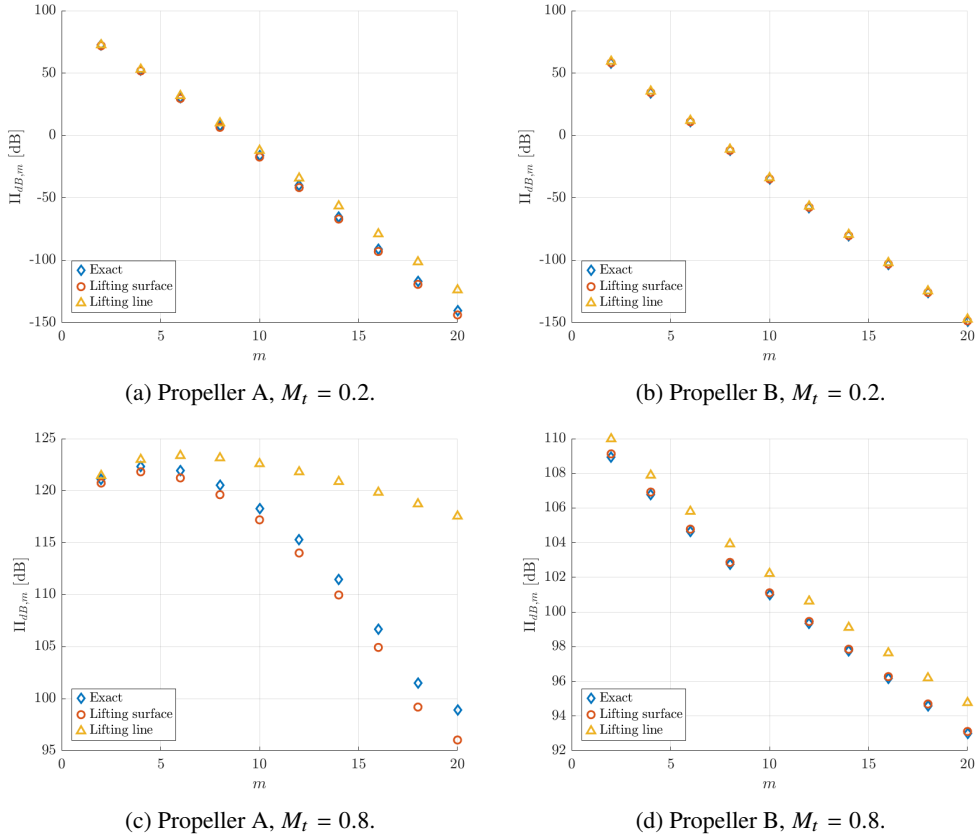


Figure 7: Acoustic power per harmonic as a function of the azimuthal index m , comparing exact surface integration with the lifting-surface and lifting-line approximations.

harmonics. However, these discrepancies occur only where the spectrum is already many tens of decibels below the first harmonic and therefore have little practical influence on the overall tonal content. At the higher tip Mach number, shown in panels 7c and 7d, the spectral decay becomes markedly weaker and a substantially larger number of harmonics contributes to the radiated power, as already anticipated in section 2.1. Under these conditions, the differences between the two reduced formulations become more informative. For Propeller A at $M_t = 0.8$, the LS approximation follows the exact trend reasonably well, although it tends to underestimate the level of the higher harmonics. By contrast, the LL approximation produces a spectrum that is too flat, with a systematic overprediction that becomes increasingly pronounced as m increases. This behaviour is consistent with the fact that, for the larger-chord propeller, finite-chord and distributed-loading effects play an important role in shaping the high-harmonic content. This is in agreement with the larger directivity error observed in panel 6c. For Propeller B at $M_t = 0.8$, the discrepancies are much smaller. The LS approximation is again almost indistinguishable from the exact solution, while the LL model shows only a nearly uniform overprediction across the spectrum. This improved behaviour is consistent with the smaller chord of Propeller B, for which compact sectional loading remains an accurate description even when the spectrum broadens. Overall, the spectral comparison complements the directivity results and confirms the expected validity trends of the two simplified models.

The time histories shown in Fig. 8 provide a complementary time-domain view of the trends

already observed in the directivity and harmonic-power comparisons. In each case, the pressure signal is evaluated in the direction of maximum radiation, at a distance $r_0 = 50R = 5$ m from the propeller centre. At the lower tip Mach number, shown in panels 8a and 8b, the waveform is nearly sinusoidal and is dominated by the first blade-passing harmonic, $m = N$. In agreement with the spectral results, both reduced models reproduce the overall periodic behaviour well in this regime. For Propeller A, the two approximations remain very close to the exact solution, with only minor differences near the extrema. For Propeller B, the agreement is very good, confirming that when the spectrum is strongly concentrated in the first few harmonics, both simplified descriptions retain the dominant acoustic content. At the higher tip Mach number, shown in panels 8c and 8d, the waveform becomes significantly more structured, with steeper gradients, sharper extrema, and visible small-scale oscillations over the main periodic variation. These features directly reflect the stronger contribution of the higher harmonics, already evident in the corresponding power spectra. In this regime, the differences between the two approximations become more pronounced. For Propeller A (panel 8c), the LS formulation still follows the exact waveform reasonably well, including the timing and overall shape of the main peaks, although some smoothing of the extrema is visible. By contrast, the LL model exhibits a marked deterioration and the pressure peaks are substantially overpredicted. For Propeller B at $M_t = 0.8$ (panel 8d), the discrepancies remain much smaller. Both reduced models preserve the correct phase and the nearly sinusoidal character of the waveform, while the LL approximation shows only a modest overprediction of the amplitude. Overall, the time-domain comparison is fully consistent with the directivity and power results.

Overall, the LL approximation is an efficient and accurate tool when the acoustic response is dominated by the first few harmonics and the main interest lies in the global tonal content. The LS approximation becomes preferable when the higher-frequency part of the spectrum has a visible impact on the waveform, since it provides a more accurate representation of the frequency structure associated with large-chord and distributed-loading effects. In addition, both approximations are advantageous in terms of computational efficiency, as their use generally leads to a reduction in computational cost. A timing benchmark was designed to isolate the cost of assembling the multipole coefficients $A_{\ell m}$, since the evaluation of pressure and radiated power involves the same steps in all formulations, namely Eqs. (2.12) and (2.13). The computational cost was assessed for propeller B at $M_t = 0.8$, retaining only the first two multipoles ($\ell_{\max} - |m| = 1$). The median execution times measured over 100 runs are 1.041×10^{-1} s for the exact surface integration, 1.783×10^{-3} s for the lifting-surface formulation, and 6.788×10^{-4} s for the lifting-line formulation. Thus, in the present implementation, both reduced models are more than one order of magnitude faster than the exact one, with speed-up factors of about 58 for LS and 153 for LL. These results are consistent with the structure of the three solutions. The LL formulation is the least expensive because, once the sectional quantities are known, the assembly reduces to spanwise operations only. The LS formulation is slightly more expensive because, in addition to the spanwise integration, it also evaluates chordwise Fourier-type integrals. However, with the present truncation $\ell_{\max} - |m| = 1$, this additional cost remains modest, since the chordwise quantities are computed once per harmonic and then reused for both retained multipoles. This explains why the difference between LS and LL is limited. The much larger cost of the exact method reflects not only the evaluation of the surface integral itself, but also all the operations required to construct and process the lofted three-dimensional blade geometry. The exact formulation is therefore penalized both by the size of the surface discretization and by the geometric preprocessing, which is absent, or considerably lighter, in the simplified formulations. As a result, the latter retain essentially the same acoustic accuracy while achieving a markedly lower computational cost.

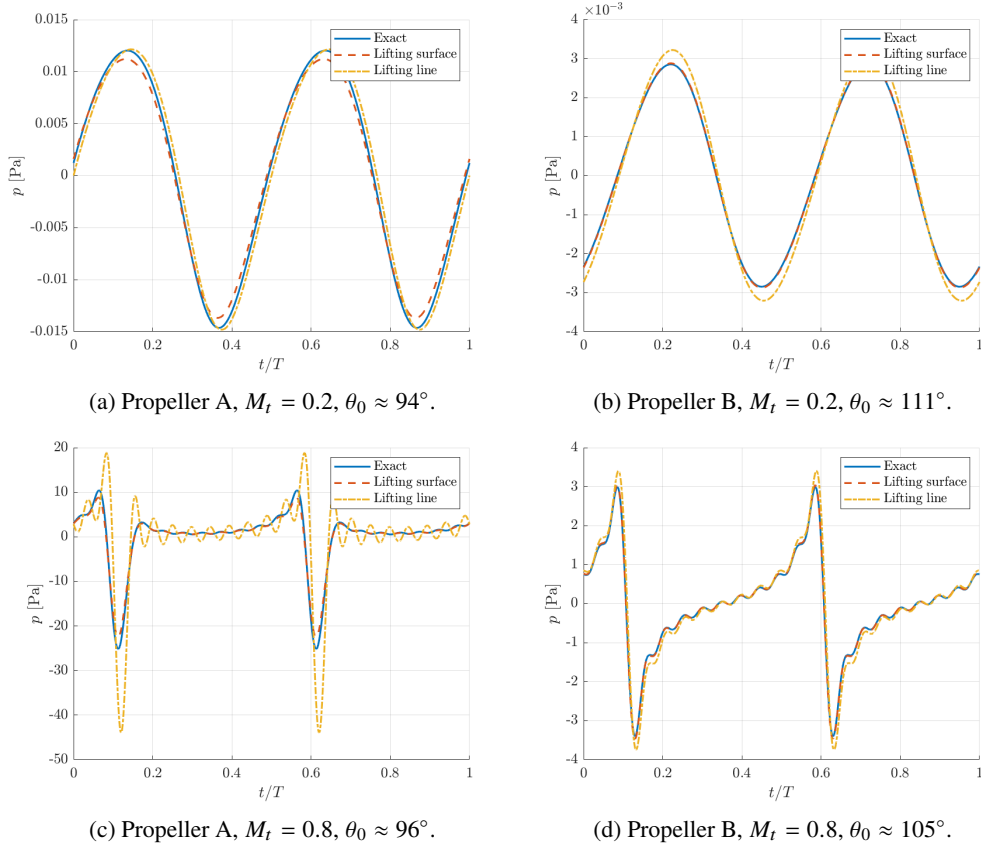


Figure 8: Far-field acoustic pressure time history over one rotor period, $T = 2\pi/\Omega$, at a fixed observer location in the meridional plane $\phi_0 = 0^\circ$, with $r_0 = 5$ m and θ_0 corresponding to the direction of maximum directivity. The results obtained from exact surface integration are compared with the lifting-surface and lifting-line approximations.

3.3.1. Lift, drag and thickness contributions

To quantify how the different physical mechanisms play a role in the multipole expansion, we decompose the radiated acoustic power to understand the contribution of the first admissible multipoles. Figure 9 reports the sound power level associated with each rotor harmonic, decomposed into the individual model contributions (different markers) and shown for two tip Mach numbers, $M_t = 0.2$ and $M_t = 0.8$ (different colours). It should be recalled that the labels “lift” and “drag” are used here only in an approximate interpretative sense. More precisely, the former corresponds to the antisymmetric contribution, associated primarily with loading normal to the reference plane, whereas the latter corresponds to the symmetric contribution, associated mainly with tangential loading.

For Propeller A, panel 9a shows that the three lifting-surface contributions remain clearly separated in level. Over most of the harmonics displayed, the thickness term is the dominant one, while the two loading-related terms remain smaller and exhibit a relative importance that varies with harmonic index. The same ordering is evident in Table 5, where for the first blade-passing harmonic the thickness contribution exceeds both the lift-related and drag-related terms at both Mach numbers. This hierarchy is consistent with the assumptions underlying the LS approximation. In the small-incidence regime on which the model is based, thickness and loading

	$M_t = 0.2$	$M_t = 0.8$
$\ell = m = 2$ (Drag)	61.2 dB	109.5 dB
$\ell = m = 2$ (Thickness)	71.5 dB	118.8 dB
$\ell = m + 1 = 3$ (Lift)	54.1 dB	115.2 dB

Table 5: Lifting-surface power contributions for the first blade-passing harmonic $m = 2$ restricted to the first two admissible multipoles ($\ell = m$ and $\ell = m + 1$) for Propeller A.

	$M_t = 0.2$	$M_t = 0.8$
$\ell = m = 2$ (Drag)	58.4 dB	108.2 dB
$\ell = m = 2$ (Thickness)	47.9 dB	95.1 dB
$\ell = m + 1 = 3$ (Lift)	50.4 dB	104.9 dB
$\ell = m + 1 = 3$ (Induced thickness)	2.9 dB	59.9 dB

Table 6: Lifting-line power contributions for the first blade-passing harmonic $m = 2$ restricted to the first two admissible multipoles ($\ell = m$ and $\ell = m + 1$) for Propeller B.

enter at comparable asymptotic order, whereas the drag-related part appears only as a higher-order correction, in agreement with thin-airfoil arguments (Ashley *et al.* 1965). For the very small angle of attack considered here ($\alpha = 2^\circ$), the blade loading remains weak enough for the thickness contribution to dominate the radiated power, while the loading terms become more visible as M_t increases. Panel 9b reports the same power decomposition for the lifting-line formulation. In this case, the hierarchy of the various contributions follows directly from the asymptotic structure of the expansion: lift and drag appear at leading order (ε_ℓ), whereas thickness enters only at the next order (ε_ℓ^2). The results reflect this ordering clearly. The dominant acoustic output is associated with lift and drag, while the thickness-related contributions remain weaker throughout the range of harmonics considered. In particular, the induced-thickness term is negligible at both Mach numbers and stays well below the other contributions.

The two approximations are based on different hypotheses and therefore capture different physical effects. Despite these differences, there exists an overlap region in which the two models predict the same leading-order multipole content. This common limit is obtained by letting the chordwise compactness parameter γ tend to zero in the LS formulation and the inflow angle φ_i tend to zero in the LL formulation. The resulting coefficient can be written as

$$I_{\ell m} = \lim_{\gamma \rightarrow 0} A_{\ell m}^{(LS)} = \lim_{\varphi_i \rightarrow 0} A_{\ell m}^{(LL,1)} = i\rho_0 a_s^2 m M_t^3 N B_{L\ell m} \int_{\bar{R}_{\text{hub}}}^1 j_\ell(m M_t \bar{r}) \gamma(\bar{r}) c_l(\bar{r}) \bar{r} e^{-im\phi_s(\bar{r})} d\bar{r} \quad (3.33)$$

Equation (3.33) shows that, in the common limit, both descriptions reduce to the same lift-generated multipole coefficient. On the LS side, the limit $\gamma \ll 1$ has two consequences. First, the chordwise phase factor $\exp\left[-im\frac{2\gamma(\bar{r})}{\bar{r}}\xi\right]$ tends to unity, so that the finite-chord interference retained by the full LS model disappears. Second, the thickness contribution, which is proportional to γ^2 , becomes asymptotically smaller than the lift term, which scales as γ . The chordwise lift integral then reduces to the sectional lift coefficient, $\int_0^1 f_L(\bar{r}, \xi) d\xi \approx c_l(\bar{r})$, and the only remaining phase information is the spanwise azimuthal factor $e^{-im\phi_s(\bar{r})}$, where ϕ_s denotes the station azimuth. In other words, once the blade becomes chordwise compact, the LS model loses

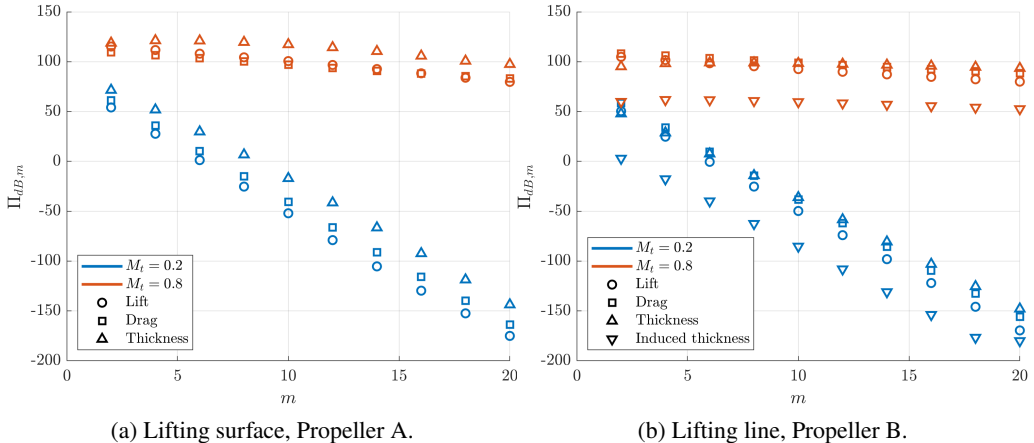


Figure 9: Sound power level $\Pi_{dB,m}$ as a function of harmonic index m , comparing the different contributions in the two approximate formulations: (a) lifting-surface (LS), with lift, drag, and thickness contributions; (b) lifting-line (LL), with lift, drag, thickness, and induced-thickness contributions.

sensitivity to the detailed loading distribution along the chord and collapses onto a spanwise lift description. On the LL side, the limit $\varphi_i \rightarrow 0$ suppresses the terms that are specific to large inflow angle. In particular, the drag-like contribution associated with the inclined sectional force vanishes, and the sectional lift direction aligns with $-\hat{\theta}$ on the plane $\theta = \pi/2$. Intuitively, the overlap region corresponds to a blade that is both slender and nearly planar: under these conditions, neither finite-chord interference nor inflow-angle corrections are strong enough to affect the acoustic field. Outside this intersection region, the two formulations differ in predictable ways, consistent with the results discussed above. From a practical standpoint, the two methods should therefore be viewed as complementary rather than competing approaches.

4. Experimental Validation

The experimental validation is omitted from the present arXiv version and will be included in the final version of the paper.

5. Conclusions

A spherical-multipole expansion has been developed for Goldstein's acoustic analogy in the particular case of rotating propellers. The main advantage of the formulation lies in the explicit separation between source and observer dependence: all source information is condensed into harmonic multipole coefficients, while the observer dependence is carried entirely by spherical harmonics and radial propagation factors. As a result, the source integrals are evaluated only once for each harmonic and multipole order, after which the acoustic field at arbitrary observer locations is recovered inexpensively, without repeated integration over the blade. This source/observer decoupling yields a clear computational advantage over formulations in which the observer coordinates remain embedded inside the source integrals. A further benefit of the multipole representation is that the radiated power can be obtained directly from the multipole amplitudes, thus providing a compact and physically meaningful measure of source strength. In the hovering subsonic regime considered here, the spherical expansion was found to converge rapidly with respect to the ℓ -index. In particular, for each harmonic the dominant far-field

radiation is generally captured by the first two non-zero multipoles, corresponding to the leading symmetric and antisymmetric contributions. This behaviour was demonstrated through coefficient decay, directivity decompositions, and reconstructed pressure fields, and explains why accurate tonal predictions can be obtained with very small truncations of the series. The resulting rapid convergence translates directly into computational savings with respect to alternative formulations available in the literature.

Two reduced descriptions of the surface integral were then introduced to clarify the physical content of the leading multipole coefficients. The first is a lifting-surface formulation, obtained by projecting the blade onto the plane of rotation. The underlying assumption is that the blade is made of thin sections operating at small incidence. The individual multipoles exhibit different symmetry properties with respect to the rotor plane: the antisymmetric family collects the lift-driven loading contribution, whereas the symmetric family collects the thickness and drag-like contributions. In the range of validity of this model, the dominant acoustic contributions are generally associated with lift and thickness, while drag usually remains secondary. The formulation retains the chordwise phase effects, which become increasingly important as the tip Mach number increases, the harmonic spectrum broadens, and the time-domain waveform departs from a sinusoidal shape. The second reduced model is a lifting-line formulation, obtained through a high-aspect-ratio expansion in which the source information is retained through compact sectional moments. In this case, no small-incidence assumption is required. The leading contribution is a force term governed by sectional lift and drag, whereas thickness enters only at a higher order. This approach loses the detailed chordwise information, but in return it is suited to more strongly twisted blades and entails a lower computational cost. Both reduced formulations result less expensive than exact surface integration while retaining the relevant acoustic content. The experimental validation is omitted from the present arXiv version and will be included in the final version of the paper.

Overall, the spherical-multipole perspective provides both physical insight and computational efficiency for tonal propeller-noise prediction. It offers a unified framework for near- and far-field analysis, while clarifying the respective roles of lift, drag, and thickness in shaping the radiated field. These features make the present approach a promising basis for fast prediction, physical interpretation, and optimization of tonal propeller noise over a broad range of operating conditions.

Appendix A. Equatorial factors

The factors $B_{L\ell m} = B_{T'_{\ell m}}$ and $B_{D\ell m} = B_{T_{\ell m}}$, which appear in the approximate expressions for the multipole coefficients, correspond to the values of the spherical harmonics and their θ -derivative evaluated on the equatorial plane. Using particular results for the associated Legendre polynomials (Abramowitz & Stegun 1972, p. 334), they can be expressed explicitly in terms of the indices ℓ and m as

$$B_{L\ell m} = B_{T'_{\ell m}} = C_{\ell m} 2^{m+1} (-4)^{-\frac{1}{2}(\ell+m+1)} \frac{(\ell+m+1)!}{\left(\frac{1}{2}(\ell+m+1)\right)! \left(\frac{1}{2}(\ell-m-1)\right)!} \quad (\text{A } 1)$$

$$B_{D\ell m} = B_{T_{\ell m}} = C_{\ell m} 2^m (-4)^{-\frac{1}{2}(\ell+m)} \frac{(\ell+m)!}{\left(\frac{1}{2}(\ell+m)\right)! \left(\frac{1}{2}(\ell-m)\right)!} \quad (\text{A } 2)$$

where $C_{\ell m} = \sqrt{\frac{2\ell+1}{4\pi} \frac{(\ell-m)!}{(\ell+m)!}}$. The above expressions are understood to be used only for admissible parity combinations of (ℓ, m) (as imposed by the symmetry of the corresponding contribution), so that the half-integer factorial arguments are non-negative integers.

Appendix B. Definition of far-field acoustic levels

The multipole expansion provides the coefficients $A_{\ell m}$. For a given azimuthal harmonic index m , the acoustic pressure amplitude \hat{p}_m and the radiated acoustic power Π_m are obtained from Eqs. (2.12) and (2.13) as series over the degree ℓ (with $\ell \geq |m|$). The complete field involves both positive and negative values of m ; however, the contributions at $\pm m$ are complex conjugates and it is sufficient to evaluate $m \geq 0$ and account for symmetry when forming total levels.

The sound pressure level (SPL) associated with the m -th harmonic is defined as

$$p_{dB,m} = 20 \log_{10} \left(\frac{\sqrt{2} |\hat{p}_m|}{p_{\text{ref}}} \right), \quad p_{\text{ref}} = 2 \times 10^{-5} \text{ Pa} \quad (\text{B } 1)$$

The overall SPL is obtained by summing the harmonic energies (Parseval's theorem)

$$p_{dB} = 20 \log_{10} \left(\frac{\sqrt{2 \sum_{m=0}^{\infty} |\hat{p}_m|^2}}{p_{\text{ref}}} \right) \quad (\text{B } 2)$$

Analogously, the sound power level associated with the m -th harmonic is

$$\Pi_{dB,m} = 10 \log_{10} \left(\frac{2 \Pi_m}{\Pi_{\text{ref}}} \right), \quad \Pi_{dB} = 10 \log_{10} \left(\frac{2 \sum_{m=0}^{\infty} \Pi_m}{\Pi_{\text{ref}}} \right), \quad \Pi_{\text{ref}} = 10^{-12} \text{ W} \quad (\text{B } 3)$$

A further quantity of interest in the far field is the directivity. The directivity of the m -th harmonic is defined as the power radiated per unit solid angle in the direction (θ_0, ϕ_0) , normalised by the average power per unit solid angle of that harmonic. It can be written as

$$D_m(\theta_0, \phi_0) = \frac{4\pi \left| \sum_{\ell=|m|}^{\infty} (-i)^{\ell+1} A_{\ell m} Y_{\ell m}(\theta_0, \phi_0) \right|^2}{\sum_{\ell=|m|}^{\infty} |A_{\ell m}|^2} \quad (\text{B } 4)$$

where the denominator is proportional to Π_m . The corresponding directivity for the total field is obtained by summing over the harmonics as in the power expression in Eq. (2.13), i.e.

$$D(\theta_0, \phi_0) = \frac{4\pi \sum_{m=-\infty}^{\infty} \frac{1}{m^2} \left| \sum_{\ell=|m|}^{\infty} (-i)^{\ell+1} A_{\ell m} Y_{\ell m}(\theta_0, \phi_0) \right|^2}{\sum_{m=-\infty}^{\infty} \frac{1}{m^2} \sum_{\ell=|m|}^{\infty} |A_{\ell m}|^2} \quad (\text{B } 5)$$

Owing to conjugate symmetry, the sums over m may be restricted to $m > 0$ when evaluating D numerically. By construction, the directivity is normalised so that its average over the sphere is unity, i.e.

$$\frac{1}{4\pi} \int_0^{2\pi} \int_0^{\pi} D(\theta_0, \phi_0) \sin \theta_0 d\theta_0 d\phi_0 = 1 \quad (\text{B } 6)$$

REFERENCES

ABRAMOWITZ, M & STEGUN, IA 1972 Handbook of mathematical functions (tenth printing ed.). *United States Department of Commerce*.

- ASHLEY, H., LANDAHL, M. & LANDAHL, M.T. 1965 *Aerodynamics of Wings and Bodies*. Dover Books on Aeronautical Engineering . Dover Publications.
- BRAMWELL, A.R.S., BALMFORD, D. & DONE, G. 2001 *Bramwell's Helicopter Dynamics*. Elsevier Science.
- BROUWER, H. 1989 A lifting line model for propeller noise. *12th Aeroacoustic Conference* .
- BROUWER, HH 1992 On the use of the method of matched asymptotic expansions in propeller aerodynamics and acoustics. *Journal of Fluid Mechanics* **242**, 117–143.
- CARLEY, M. 1999 Sound radiation from propellers in forward flight. *Journal of Sound and Vibration* **225** (2), 353–374.
- CARLEY, MICHAEL 2006 Series expansion for the sound field of rotating sources. *Tb SFW Pages* **20**, 1252–1256.
- CHAPMAN, C. J. 1993 The structure of rotating sound fields. *Proceedings of the Royal Society of London. Series A: Mathematical and Physical Sciences* **440** (1909), 257–271.
- CRIGHTON, D. G. & PARRY, A. B. 1991 Asymptotic theory of propeller noise. ii - supersonic single-rotation propeller. *AIAA Journal* **29** (12), 2031–2037, arXiv: <https://doi.org/10.2514/3.10838>.
- CROW, S. C. 1970 Aerodynamic sound emission as a singular perturbation problem. *Studies in Applied Mathematics* **49** (1), 21–46.
- CURLE, N. 1955 The influence of solid boundaries upon aerodynamic sound. *Proceedings of the Royal Society of London. A. Mathematical and Physical Sciences* **231** (1187), 505–514, arXiv: <https://royalsocietypublishing.org/rspa/article-pdf/231/1187/505/49194/rspa.1955.0191.pdf>.
- DEMING, A FM' 1937 Noise from propellers with symmetrical sections at zero blade angle. *Tech. Rep.* .
- DOBZYNSKI, W. 1993 Propeller noise reduction by means of unsymmetrical blade-spacing. *Journal of Sound and Vibration* **163** (1), 123–126.
- DOUGLAS MAST, T. & YU, FENG 2005 Simplified expansions for radiation from a baffled circular piston. *The Journal of the Acoustical Society of America* **118** (6), 3457–3464.
- DRELA, MARK 1989 *XFOIL: An Analysis and Design System for Low Reynolds Number Airfoils*.
- FARASSAT, F. 1977 Discontinuities in aerodynamics and aeroacoustics: The concept and applications of generalized derivatives. *Journal of Sound and Vibration* **55** (2), 165–193.
- FARASSAT, FERI 1981 Linear acoustic formulas for calculation of rotating blade noise. *AIAA journal* **19** (9), 1122–1130.
- FARASSAT, FERI & SUCCI, GEORGE P 1980 A review of propeller discrete frequency noise prediction technology with emphasis on two current methods for time domain calculations. *Journal of Sound and Vibration* **71** (3), 399–419.
- FFOWCS WILLIAMS, J.E. & HAWKINGS, D.L. 1969 Theory relating to the noise of rotating machinery. *Journal of Sound and Vibration* **10** (1), 10–21.
- FFOWCS WILLIAMS, J. E. & HAWKINGS, D. L. 1969 Sound generation by turbulence and surfaces in arbitrary motion. *Philosophical Transactions of the Royal Society of London, Series A: Mathematical and Physical Sciences* **264** (1151), 321–342, arXiv: <https://royalsocietypublishing.org/rsta/article-pdf/264/1151/321/267806/rsta.1969.0031.pdf>.
- FRUNCILLO, FELICE, LUCHINI, PAOLO & GIANNETTI, FLAVIO 2025 Multipole expansion approach for rotor noise prediction. *Journal of Sound and Vibration* **617**, 119317.
- GARRICK, I. E. & WATKINS, CHARLES E. 1954 A theoretical study of the effect of forward speed on the free-space sound-pressure field around propellers. *NASA Technical Report* .
- GLEGG, STEWART & DEVENPORT, WILLIAM 2024 6 - propeller and open rotor noise. In *Aeroacoustics of Low Mach Number Flows (Second Edition)*, Second edition edn. (ed. Stewart Glegg & William Devenport), pp. 163–206. Academic Press.
- GLEGG, STEWART A. L. 1991 Effect of centerbody scattering on propeller noise. *AIAA Journal* **29** (4), 572–576.
- GOLDSTEIN, M.E. 1976 *Aeroacoustics. Advanced book program* . McGraw-Hill International Book Company.
- GUTIN, L 1936 On the sound field of a rotating propeller. *Physikalische Zeitschrift der Sowjetunion: Physical magazine of the Soviet Union volume 9 number 1 (translated as 1948 NACA Tech. Memo. 1195)* .
- HANSON, D. 1976 *Near field noise of high tip speed propellers in forward flight*, chap. ., pp. ., ., arXiv: <https://arc.aiaa.org/doi/pdf/10.2514/6.1976-565>.
- HANSON, DONALD B. 1980 Helicoidal surface theory for harmonic noise of propellers in the far field. *AIAA Journal* **18** (10), 1213–1220.
- HANSON, DONALD B. 1983 Compressible helicoidal surface theory for propeller aerodynamics and noise. *AIAA Journal* **21** (6), 881–889, arXiv: <https://doi.org/10.2514/3.60132>.

- HANSON, DONALD B. 1985 Near-field frequency-domain theory for propeller noise. *AIAA Journal* **23** (4), 499–504.
- HANSON, DONALD B & FINK, MARTIN R 1979 The importance of quadrupole sources in prediction of transonic tip speed propeller noise. *Journal of Sound and Vibration* **62** (1), 19–38.
- HANSON, DONALD B & PARZYCH, DAVID J 1993 Theory for noise of propellers in angular inflow with parametric studies and experimental verification. *Tech. Rep.*. NASA. Lewis Research Center.
- HAWKINGS, D.L. & LOWSON, M.V. 1974 Theory of open supersonic rotor noise. *Journal of Sound and Vibration* **36** (1), 1–20.
- HUBBARD, HARVEY H 1991 Aeroacoustics of flight vehicles: Theory and practice volume 1: Noise sources. *Aeroacoustics of Flight Vehicles: Theory and Practice* **1** (WRDC-TR-90-3052-VOL-1).
- JACKSON, J.D. 1962 *Classical Electrodynamics*. Wiley.
- JOHNSON, WAYNE 2013 *Rotorcraft aeromechanics*, , vol. 36. Cambridge university press.
- KHERSONSKIL, VALERY KELMANOVICH, MOSKALEV, ANATOLY NIKOLAEVICH & VARSHALOVICH, DMITRY ALEXANDROVICH 1988 *Quantum theory of angular momentum*. World Scientific.
- LIGHTHILL, MICHAEL JAMES 1952 On sound generated aerodynamically i. general theory. *Proceedings of the Royal Society of London. A. Mathematical and Physical Sciences* **211** (1107), 564–587, arXiv: <https://royalsocietypublishing.org/rspa/article-pdf/211/1107/564/45649/rspa.1952.0060.pdf>.
- METZGER, FREDERICK B. 1995 A review of propeller noise prediction methodology: 1919-1994. *Tech. Rep.* Report Number: NAS 1.26:198156. NASA.
- MORFEY, CL 1972 The acoustics of axial flow machines. *Journal of Sound and Vibration* **22** (4), 445–466.
- MORFEY, CL 1973 Rotating blades and aerodynamic sound. *Journal of Sound and Vibration* **28** (3), 587–617.
- PARRY, A. B. & CRIGHTON, D. G. 1989 Asymptotic theory of propeller noise. i - subsonic single-rotation propeller. *AIAA Journal* **27** (9), 1184–1190, arXiv: <https://doi.org/10.2514/3.10244>.
- SCHULTEN, B. H. M. 1984 Aeroacoustics of wide-chord propellers in non-axisymmetric flow. *9th Aeroacoustics Conference, AIAA* , arXiv: <https://arc.aiaa.org/doi/pdf/10.2514/6.1984-2304>.
- TREBBLE, W. J. G. 1987a Investigation of the aerodynamic performance and noise characteristics of a 1/5th scale model of the dowty rotol r212 propeller. *The Aeronautical Journal* **91** (905), 225–236.
- TREBBLE, W. J. G. 1987b Investigations of the aerodynamic performance and noise characteristics of a dowty rotol r212 propeller at full-scale in the 24 ft wind tunnel. *The Aeronautical Journal* **91** (906), 275–284.
- WILLIAMS, EARL G 1999 *Fourier acoustics: sound radiation and nearfield acoustical holography*. Elsevier.
- ZHONG, SIYANG, ZHOU, PENG, FATTAH, RYU & ZHANG, XIN 2020 A revisit of the tonal noise of small rotors. *Proceedings of The Royal Society A* **476**, 20200491.